Picosecond optical pulses by electro-optic laser modulation for single photon generation

Kuijf, Ilse

Picosecond optical pulses by electro-optic laser modulation for single photon generation

THESIS

submitted in partial fulfillment of the
requirements for the degree of

MASTER OF SCIENCE
in
PHYSICS

Author :	I.S. Kuijf
Student ID :	S2024802
Supervisor :	Dr. W. Löffler, P. Steindl
Second corrector :	Dr. A. Morin

Leiden, The Netherlands, August 23, 2022

Picosecond optical pulses by electro-optic laser modulation for single photon generation

I.S. Kuijf

Huygens-Kamerlingh Onnes Laboratory, Leiden University
P.O. Box 9500, 2300 RA Leiden, The Netherlands

August 23, 2022

Abstract

Efficient single-photon sources based on semiconductor quantum dots typically rely on resonant excitation schemes with a high degree of control. In particular, having access to continuous-wave (CW) and pulsed excitation without changing the center frequency is highly desirable. CW excitation is useful for alignment and characterization, while pulsed excitation is essential for on-demand single-photon production.

We present a technique based on ultra-fast electro-optic modulation to directly synthesize optical pulses from a narrow linewidth CW laser. With custom-built ultra-fast electronics, we demonstrate tunable pulse lengths down to 50 ps. Pulses longer than 100 ps achieve a typical extinction ratio of 300, and the 50 ps pulses still show an extinction ratio of 150. We then use these pulses to excite a single InAs quantum dot in a micropillar cavity and show the generation of true single photons. This technique allows for full control over the experiment in the temporal-spectral domain, and is significantly simpler compared to using conventional Ti:Sa mode-locked laser oscillators in combination with grating-based pulse shaping.

Contents

Chapter 1

Introduction

Photons are the elementary quantum particles of light. If one can manage to control these photons on the single-photon level, a whole world of applications opens up. In particular, single photons are a key component of many quantum information protocols [1–3]. One way to generate single photons is by resonant excitation of a semiconductor quantum dot (QD). In the resonant regime, a QD can be pictured as a two-level system that emits a photon upon spontaneously decaying to its ground state after being excited. Since the emission is spontaneous, i.e. in all directions, the collection efficiency of single-photon sources based on bare QDs is limited. Therefore, the QD is often embedded into an optical microcavity, such as a micropillar cavity [4–6], allowing near unity coupling of the QD into propagating optical modes and thus enhancing the collection efficiency. This is the domain of cavity-QED (quantum electrodynamics).

To identify the cavity resonance frequency with high precision, often a narrow linewidth continuous-wave (CW) tunable laser is used. However, for applications requiring true single photons on demand, pulsed excitation is necessary. With pulsed excitation using sufficiently short pulses, the QD can only be excited once within the pulse. This ensures the generation of at maximum one photon per pulse. The pulses should not be too short, as due to the Heisenberg spectral-temporal uncertainty principle a shorter pulse will have a broadened spectrum, leading to a worse coupling with the cavity-QED system. The pulse length should thus be comparable with the lifetime of the emitter we want to address. The typical reported lifetimes for InAs QDs coupled to micropillar cavities are of order 100 ps [6], meaning that the pulses should be fine-tunable in the tens of ps range.

In an experimental cavity-QED setup it is thus desired to have highly wavelength and pulse-length tunable lasers allowing both pulsed and continuous excitation. However, since these lasers do not exist, one typically switches between multiple lasers, leading to a disruption of optimal excitation settings. A common approach is to use a CW titanium-sapphire (Ti:sapphire) laser oscillator with mode-lock possibility to generate ultrashort few-ps pulses. However, fine-tuning the pulse length requires grating-based pulse shaping [7]. Furthermore, these lasers offer little control over the repetition rate of the pulses. Another approach is to use phase modulation to manipulate the laser light. A fast phase modulator based on $LiNbO_3$, in combination with a fast programmable electronic pulse-pattern, can be used to directly modulate a CW laser to a pulsed laser [8, 9]. This technique allows tuning the central wavelength and pulse shape without the need for a pulsed laser, where the time domain is only limited by the electronics and the extinction ratio of the modulator.

In this thesis, we present a similar technique based on ultra-fast electro-optic intensity modulation in combination with custom-built ultra-fast electronics to directly modulate optical pulses from a narrow linewidth CW laser. Measurements of the second-order correlation function of the pulsed light are used to reconstruct the pulse durations and extinction ratios. The necessary theory behind electro-optic modulation, the fast electronics, and the second-order correlation function is given in Chapter 2. In Chapter 3 we show photon correlations simulations. The methods and results of the experimental characterization of the pulse modulator are given in Chapter 4. Finally, in Chapter 5 we demonstrate the generation of true single photons by using the pulse modulator to do pulsed resonance fluorescence with a single InAs/GaAs quantum dot in an optical microcavity.

Chapter 2

Theory

To directly modulate a continuous-wave laser into a pulsed laser, an electro-optic intensity modulator is used. The theory needed to understand the functionality of this modulator is presented in Section 2.1. The custom-built fast electronics that are needed to generate the ps pulses are explained in Section 2.2. The principle behind the experiment to characterize the pulses is explained in Section 2.3. Finally, Section 2.4 explains the theory needed to analyze the single-photon experiments.

2.1 Electro-optic intensity modulator

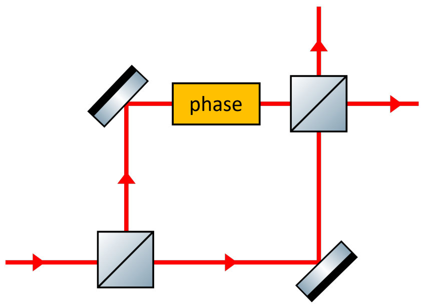

Figure 2.1: *Basic Mach-Zehnder interferometer.*

The continuous wave laser light is modulated with a Mach-Zehnder type optical modulator. A basic Mach-Zehnder scheme is shown in Figure 2.1. In a Mach-Zehnder interferometer, the input light is split into two paths, after which a phase difference is induced between the two paths. The two paths are then recombined at the output to get constructive or destructive interference, depending on the phase difference. The interference can be used to modulate continuous wave laser light to obtain pulsed laser light, by rapidly changing the phase difference between constructive interference and destructive interference. The intensity difference between the pulse light and the inter-pulse dark is then determined by the extinction ratio of the interferometer. The extinction ratio ER is given by Equation 2.1.

$$ER(dB) = 10\log_{10}\left(\frac{P_{max}}{P_{min}}\right), \qquad ER = \frac{P_{max}}{P_{min}} \tag{2.1}$$

Th ER is the ratio between the optical output power of the modulator at constructive interference P_{max}, and the optical output power at destructive interference P_{min}. The maximum repetition rate and shortest pulse length that can be achieved with the modulator are determined by the pulse rise time. The pulse rise time is the time it takes the leading edge of a pulse to rise from 10% to 90% of its maximum value.

The optical modulator used in this thesis is a commercial waveguide type $LiNbO_3$ Mach-Zehnder optical modulator. This is an electro-optic intensity modulator (EOM) with a typical ER of 25 dB, or $\sim$300, and pulse rise time less than 20 ps. In this device, the input fiber is coupled to a waveguide, which is then split into two paths using a waveguide splitter. Between the two paths, a phase difference is induced through the linear electro-optic effect, also called the Pockels effect. This effect results in a change of the refractive index of a crystal in response to an electric field. The EOM consists of a transverse Pockels cell, which is an electro-optic crystal through which light can propagate [10]. In the EOM used in this thesis, the electro-optic crystal is lithium niobate ($LiNbO_3$). Since $LiNbO_3$ crystals are naturally birefringent, it is important to only consider linear polarization along the Z axis of the crystal [11].

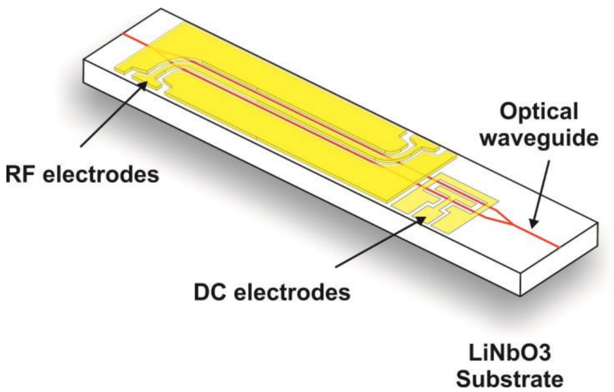

Figure 2.2: *Schematic view of a $LiNbO_3$ intensity modulator chip. From iXblue [12]*

The electric field which changes the phase of the light is applied with electrodes. The EOM used in this thesis has two sets of electrodes, as indicated in Figure 2.2 [12]. The bias electrodes, or DC electrodes, are used to set a bias voltage to determine the operating point of the device. The modulation electrodes, or RF electrodes, are used to then modulate the intensity at very high frequencies. In order to create pulses, the bias is set to have destructive interference at the output. The RF signal is a periodic pulse train, to obtain a periodically pulsed laser. The transfer function of the Mach-Zehnder type EOM is given by Equation 2.2.

$$I_{out} = T_{mod}\frac{I_{in}}{2}\left[1+\cos\left(\frac{\pi}{V_\pi}V(t)-\phi\right)\right] \tag{2.2}$$

Here I_{in} and I_{out} are the input and output intensity, T_{mod} is the optical transmission of the device, V_π is the half-wave voltage and $V(t)$ is the applied voltage. The ϕ term is a phase term which arises from small differences between the two optical paths due to material inhomogeneity and manufacturing tolerances.

2.2 Pulser electronics

To modulate the continuous wave laser into a pulsed laser, an electrical periodic pulse train has to be applied to the RF electrodes of the EOM (see Sec. 2.1). To do this, fast electronics which can generate extremely short pulses of the order of 30 ps are required. In order to have a flexible system with full access to the electronics, the electronics needed to achieve such fast pulses were developed by the university's electronics department (ELD) by Harry Visser and Arno van Amersfoort. A block diagram of the full electronic circuit is shown in Figure 2.3. The main part of the electronics is a fast pulse PCB which is driven by a field-programmable gate array (FPGA). A microcontroller is responsible for the communication between the PC and the FPGA.

The FPGA contains the control logic and can be used to set the pulse pattern. It contains a fast and a slow pulse generator to allow for a broad range of pulse possibilities. The slow pulse generator can generate pulses between 20 ns and 650 ms, with repetition rates ranging from 1.5 Hz to 25 MHz. The fast pulse generator creates programmable pulse patterns with a resolution of 1 ns and a repetition rate between 8.33 MHz and 500 MHz. In our case, the FPGA generates fast long pulses of 1 ns at the desired repetition rate of around 50 MHz. These 1 ns pulses are then compressed into short pulses of the desired pulse duration by the pulse compressor on the pulse PCB.

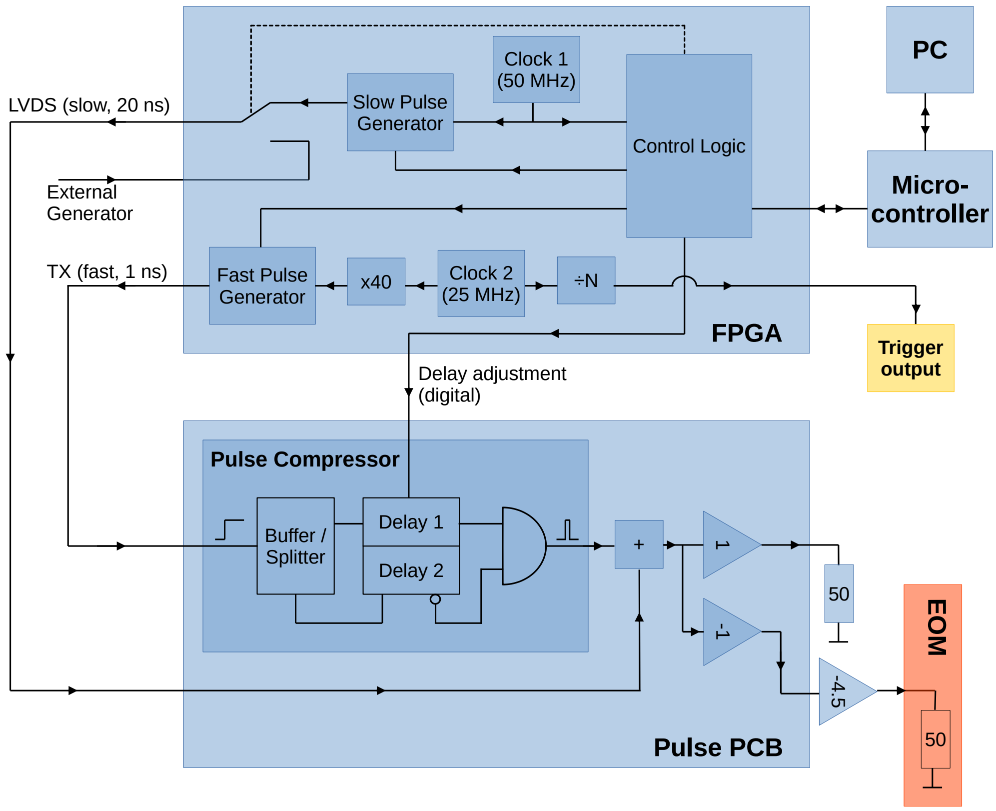

__Figure 2.3:__ Schematic block diagram representing the pulser electronics. Long pulses are created by the FPGA at the desired frequency, which are then compressed to the desired lengths by the pulse compressor on the pulse PCB. Adapted from the Leiden university ELD.

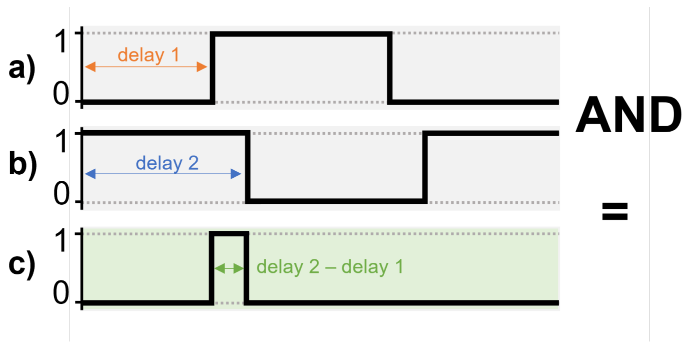

__Figure 2.4:__ Schematic of how the short pulses are created in the Pulse compressor. Figure (a) shows the long pulse in delay line 1, (b) shows the inverted long pulse in delay line 2 and (c) shows the resulting short pulse after the AND gate.

Figure 2.4 shows a simplified schematic of how this is done. The 1 ns pulse is split into two paths by the splitter. The two resulting signals are then fed through two delay lines with programmable delay times. These delay times can be set between 0 and 5 ns and have a 5 ps resolution. The long pulse on delay line 2 is inverted, and added to the long pulse of delay line 1 through an ultra-fast AND gate. An AND gate only produces a 1 if the value on both inputs is 1. As can be seen in Figure 2.4, this results in a short pulse at the output of the AND gate, where the length of the pulse is determined by the difference between the delay lines. In reality, also the difference in length of the signal paths to delay 1 and delay 2 have to be taken into account, which results in an extra offset in the "delay 2 - delay 1" metric. The values for delay 1 and delay 2 are key parameters of the pulser electronics, and form the basis of the experiments done to characterise the pulse modulator.

The FPGA also produces trigger pulses which can be useful for some experiments. For this trigger output, the frequency has to be manually set using the `syncdiv` parameter. The frequency of the trigger pulses will then be $f_{trigger} = \frac{25\,\text{MHz}}{\texttt{syncdiv}}$.

2.3 Second-order correlation function

The shortest laser pulses produced by the modulator are, hopefully, around 30 ps long. For longer pulses, an approach to characterize the pulses could be to directly measure them with a detector. However, for laser pulses this short, this would require ultrafast ps-scale detectors which are not readily available. Therefore we use single-photon detectors with a ps-scale timing jitter. With single-photon detectors, we have to take into account the detection probability, timing jitter and dead time. The timing jitter is the fluctuation in the temporal position of the detection event. The dead time is the minimum time it takes the detector to recover after a detection event. No events can be detected during this dead time. Typical dead times for single photon detectors are of the order of tens of nanoseconds and typical timing jitters are of the

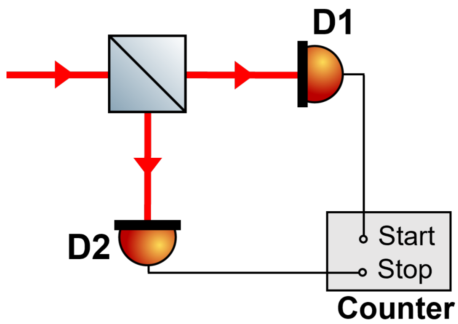

Figure 2.5: Schematic of a HBT setup using start-stop operation. The red arrows indicate the direction of the light and the orange half-circles are the detectors D1 and D2.

order of tens of picoseconds. This means that directly detecting a pulse shape of ∼30 ps is impossible. A way to bypass the long dead time and characterize short laser pulses is to use a Hanbury-Brown Twiss setup.

A Hanbury-Brown Twiss (HBT) setup makes use of a beam splitter and two detectors to measure the second-order correlation function $g^{(2)}(\tau)$. The second-order correlation function quantifies the intensity fluctuations of a signal, and is generally given by Equation 2.3 [13].

$$g^{(2)}(\tau) = \frac{\langle I_1(t) I_2(t+\tau)\rangle}{\langle I_1(t)\rangle \langle I_2(t+\tau)\rangle} \tag{2.3}$$

Here, $I(t)$ is the intensity of the light at time t. The subscript indicates the detector on which the light is incident. The angled brackets indicate the time average computed by integrating over a long period. This expression is normalized such that perfect coherent light has a value of $g^{(2)}(\tau) = 1$ everywhere.

A typical HBT setup for photons, shown in Figure 2.5, works by measuring the time delays τ between clicks on the two detectors (D1 and D2). These time delays are then binned into a histogram by a counter to obtain the second-order correlation function. This measurement can typically be done in two ways. One is to use start-stop operation, where a detection event on D1 starts the timer and a detection event on D2 stops the timer. This method only measures time differences of consecutive photon detection events, and results in a histogram of coincidence counts $K(\tau)$. The other way is to record all timestamps of all detections on D1 and D2, and then cross-correlate the two signals with each other. This means that for each event on D1, all time differences τ with all events on D2 are calculated. This will result in a histogram of coincidence counts $J(\tau)$ of all photon detection combinations.

This thesis uses two different counting cards, of which one uses start-stop operation and the other full cross-correlation. In both cases the measurement returns a histogram of coincidence counts as function of the time difference τ. This means that in the photon-counting setup, the intensity $I(t)$ of Equation 2.3 has to be represented as a discrete number of photons. This results in Equation 2.4, where $n_i(t)$ denotes the number of counts registered on detector i at time t. Since our detectors are not photon number resolving, $n_i(t)$ will be 0 or 1 for each time bin.

$$g^{(2)}(\tau) = \frac{\langle n_1(t) n_2(t+\tau)\rangle}{\langle n_1(t)\rangle \langle n_2(t+\tau)\rangle} \tag{2.4}$$

Since the coincidence counts are binned into a histogram, time is discretized in steps of Δt. This means the time averages can be written as discrete Riemann sums:

$$g^{(2)}(\tau) = \frac{\frac{1}{N}\sum_{i=1}^{N} n_1(t)n_2(t+\tau)}{\frac{1}{N^2}\left(\sum_{i=1}^{N} n_1(t)\right)\left(\sum_{i=1}^{N} n_2(t+\tau)\right)} = N\frac{J(\tau)}{SC_1\ SC_2} \tag{2.5}$$

Here $N = \frac{T_{tot}}{\Delta t}$ is the number of bins, or timestamps, of n_1 and n_2. SC_i represents the total number of individual single counts on detector i. It can be seen that $J(\tau)$ is directly proportional to $g^{(2)}(\tau)$. This means that for the full cross-correlation method, $g^{(2)}(\tau)$ can be obtained from $J(\tau)$ by normalizing the coincidence counts with a factor $\frac{N}{SC_1\ SC_2}$.

For start-stop operation, the conversion to $g^{(2)}(\tau)$ is more complicated. Firstly, a lot of photon pair-correlations are missed, which results in less coincidence counts. Secondly, if the time differences τ of interest are of the same order of magnitude as the times between clicks, then the larger τ values might never be recorded. A correction consisting of an infinite sum of self-convolutions would be needed to correct for this [14, 15]. However, if $\tau \ll R^{-1}$ with R the photon click rate, then it can be approximated that $K(\tau) \sim J(\tau)$. In our experiments, R is of the order of 10^6 detections/sec and we are interested in τ of the order of ns. This means the condition is well satisfied and no correction should be needed for the start-stop results. The problem of how to formally normalize $K(\tau)$ to $g^{(2)}(\tau)$, and $g^{(2)}(\tau)$ normalization for pulsed light in general, will be further addressed in Chapter 3.

2.4 Single photon sources

For coherent light, $g^{(2)}(\tau) = 1$ for all τ. However, for single photon light a dip around $g^{(2)}(0)$ can be expected. This dip is caused by the finite lifetime τ_r of the QD. The lifetime is the characteristic time it takes the QD to be re-excited after emission of a photon. Due to this time, for a pure single photon source there will never be two photons generated at the same time. There will thus always be at least some time delay between two consecutive photons. In the HBT setup, this means that at $\tau = 0$, for perfect detectors without jitter, there should be no photon correlations. A relation that can be used to describe this dip is given in Equation 2.6.

$$g^{(2)}_{2L}(\tau) = 1 - \exp(-\tau/\tau_r) \tag{2.6}$$

This equation describes photon correlations from a perfect two-level system. If $g^{(2)}$ shows bunching, a three-level system with an additional dark state might be a better model [6]. However, the $g^{(2)}$ measurements in this thesis do not show significant anti-bunching, so the simple formula of Eq. 2.6 can be used.

Chapter 3

Simulation of photon correlations with realistic detectors

To get a feeling for what to expect of the HBT measurement of the laser pulses, a simple simulation can be done. With the simulation presented in this chapter, different pulse shapes and detector settings can easily be tested to help understand the experimental data. The code can also be easily modified to simulate other experiments which involve a stream of light and one or more realistic detectors. The simulation assumes photons are classical particles, and does not support quantum interference effects.

3.1 Methods

The simulation is based on the simulations by Schneider et al. [16], who simulate a realistic thermal light stream and HBT experiment. To simulate the thermal light stream, they discretize time and generate a number of photons for each time bin (including 0 photons). To simulate a realistic experiment they include numerous detector effects such as dead time and timing jitter. In this thesis, the code for the realistic experiment follows the approach by Schneider et al. [16]. The simulation of the photon stream is modified to simulate coherent (pulsed) light. All code is written in Python 3.6.12, using the `Numpy` library.

3.1.1 Stream of pulsed coherent light

In the simulation performed in this thesis, time is discretized in very small time steps of Δt ($\sim$ 1 fs). This results in most time bins being empty, i.e.

containing no photons. To save memory space and thus computation time, the timestamps of the individual photon detection events are stored, instead of the number of photons for each time bin. These timestamps are stored as integers in units of Δt, to ensure the simulation has the desired time resolution. This means the maximum simulation time is the largest possible integer (for Numpy's `int64`, this is $9 \cdot 10^{18}$), multiplied with the time discretization Δt. The size of the array representing the stream of light will then be the total number of photons. The simulated timestamps represent the times on which the photons would be detected by a perfect detector.

To simulate coherent light, we assume a Poisson process. For a Poisson process, the average time between detection events is known, but the individual events are independent of each other and thus randomly spaced. The Poisson probability distributions for the number of photons and interarrival times are given in Equations 3.1 and 3.2, respectively [13].

$$P_k(\Gamma, T) = e^{-\Gamma T} \frac{(\Gamma T)^k}{k!} \tag{3.1}$$

$$P_t(\Gamma) = e^{-\Gamma t} \tag{3.2}$$

Here, P_k represents the probability to observe k photons in a time period T, and P_t represents the probability to observe at least a time t between two photons. Γ is the average rate of photons, which is a measure of the intensity of the light. This distribution can easily be achieved by randomly distributing the number of photons over the time interval. Pulsed coherent laser light is simulated by drawing a number of photons for each pulse from the Poisson distribution shown in Equation 3.1, and randomly distributing them over the pulse interval. Note that this simulates perfect block pulses, while in reality the ultrashort ps-pulses are expected to have a Gaussian shape. To create a Gaussian shape, the timestamps have to be drawn from a normal distribution with the FWHM equal to the pulse length. The resulting statistics for the light in the simulated block pulses are shown in Figure 3.1, which indeed follow the desired distributions of Equations 3.1 and 3.2.

To simulate a realistic light stream, background light can be added on top of the pulsed light. This is done by randomly distributing a number of background photons over the entire simulated light stream.

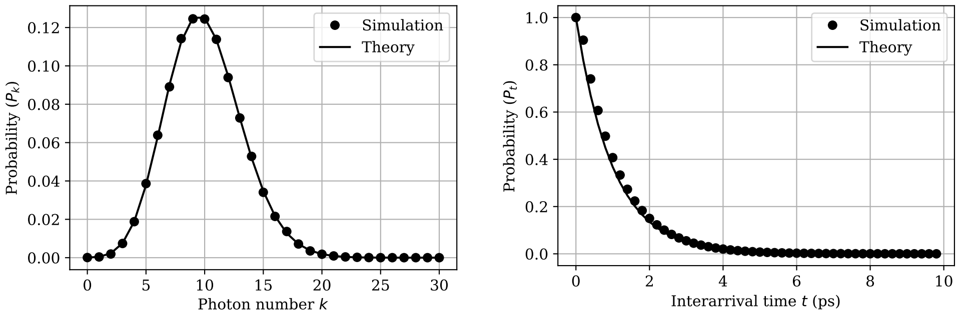

***(a)** Photon number distribution* ***(b)** Interarrival time distribution*

***Figure 3.1:** The Poissonian statistics of the simulated coherent light. This light stream consisted of* 10^6 photons*, with* $\Gamma = 10^{12}$ photons/sec *and* $\Delta t = 1$ fs*. The dots represent the simulation and the solid line the theory from Equations 3.1 and 3.2. Figure (a) shows the photon number distribution for a counting time of* 10 ps *and (b) shows the interarrival time distribution.*

3.1.2 Realistic detectors

To simulate realistic HBT measurements, the beam splitter (BS) is simulated by randomly determining for each photon in the original light stream which detector it will hit, based on a certain splitting ratio of the BS. The splitting ratio is taken to be 0.5. This results in two light streams which are detected by the two realistic detectors. A realistic detector can be simulated by incorporating a number of effects. One is the quantum efficiency η of the detector, which is the chance that an incident photon on the detector results in a detection event. A random number $r \in [0, 1)$ is generated for each photon timestamp, and the timestamp is deleted from the array if $r > \eta$. Since for our experiment this effectively just lowers the intensity of the light, η could be set to 1 to save computation time.

The second effect is the timing jitter t_{jitter} of the detector. This is a temporal uncertainty which is added to each detection event. The timing response of a detector typically follows a Gaussian shape, where t_{jitter} is defined as the FWHM of the response. A random time delay is added to each timestamp, drawn from a Gaussian distribution with standard deviation $t_{jitter}/2.355$. The factor 2.355 is due to the definition of t_{jitter} as the FWHM of the shape. The assumed Gaussian distribution is centered around $t = 0$, as adding an offset would not change the time differences between the detected photons. For the simulation we assume a jitter of $t_{jitter} = 60$ ps. Note that for the analysis of the experimental data in Chapter 4, a more realistic timing response is used, which includes an exponential diffusion tail. However, for this simulation a Gaussian distribution is sufficient.

The third effect is the dead time t_{dead} of the detector. This is the time it takes the detector to recover after a detection event. During this time, the detector will not detect any photons. There are two simple dead time models, depending on if the detector is paralyzable or nonparalyzable [17]. For a paralyzable detector, a photon hitting the detector during the dead time leads to an elongation or reset of the dead time period. For a nonparalyzable detector, photons hitting the detector during the dead time do not influence the dead time period. For the SPADs used in this thesis, we assume nonparalyzable behaviour with a typical dead time of $t_{dead} = 50$ ns. This means that after each detection, any photons which hit the detector within 50 ns are ignored.

A fourth detector effect is after pulsing, which is a small chance to have a second spurious detection pulse after a real detection pulse. Since this effect can often be neglected, it is not included in the simulation performed in this thesis.

To simulate accurate detection conditions, the time-to-digital converter (TDC) of the setup is also simulated. This is a device which triggers to the flanks of the pulses produced by the detectors to measure the time differences between the detection events. The TDC bins the time differences into bins with a certain time resolution Δt_{TDC}. This time resolution has to be taken into account in the simulation when simulating the HBT measurement. Two different TDCs are used in this thesis; a Chronologic HPTDC8-PCI with 25 ps resolution and a Becker-Hickl SPC-330 with 3 ps resolution. In the simulation a resolution of 10 ps is used.

3.2 Results

The simulation can be used to gain understanding of $g^{(2)}(\tau)$ for pulsed light. The results of this are shown in Section 3.2.1. The simulation can also be used to study the consequences of the different detector effects on the measured $g^{(2)}(\tau)$. The results of this study are presented in Section 3.2.2. Finally, the simulation is used to study the difference between start-stop operation and full cross-correlation of the signal, the results of which are shown in Section 3.2.3.

3.2.1 Second-order correlation function for pulsed light

Section 2.3 explained how to normalize the measured histogram of coincidence counts $J(\tau)$ to a proper $g^{(2)}(\tau)$. For pulsed light, $g^{(2)}(\tau)$ can be expected to consist of a number of peaks, separated by the period T of the pulses. One might expect that the peaks are at $g^{(2)} = 1$. However, as can be seen in Figure 3.2, this is not the case for a simulation of a properly normalized $g^{(2)}(\tau)$. This can be explained with the general definition of $g^{(2)}(\tau)$ (Eq. 2.3). Formally, $g^{(2)}(\tau)$ is normalized with the average intensity of the light. For pulsed light, this average intensity is a lot lower than the intensity at the pulses. Hence, the peaks of pulsed light in $g^{(2)}(\tau)$ have a value $\gg 1$, which depends on the period and length of the pulses. To have the peaks at $g^{(2)} = 1$, the function should be normalized with the average intensity of the pulses. This would be a tedious calculation involving the pulse shape, pulse duration and period of the pulses, with the end result being that the peaks have a value of 1. If this is the desired result, one might as well directly normalize the peaks to 1, as is often done in experimental work and will also be done in this thesis.

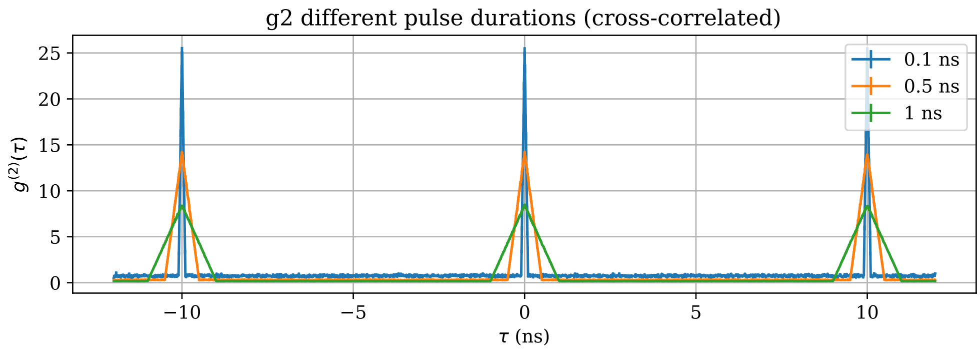

Figure 3.2: *Simulation for three block pulses of different durations, simulated for* 1 ms *with a period of* 10 ns*, an intensity of* 10^{10} photons/sec*,* 1% *background light and perfect detectors.*

3.2.2 Different detector effects

In the simulation shown in Figure 3.2, no detector effects were incorporated. Figure 3.3 shows how the different detector effects affect the measured $g^{(2)}(\tau)$. Here the light was simulated with an intensity of 10^{10} photons/sec at the peaks. The background light was set to 10^7 photons/sec, so that the pulses have an extinction ratio of 1000. Since the period was 100 ns and the pulse duration 100 ps, this corresponds to a total measured intensity of 10^6 photons/sec when the quantum efficiency of 0.05 is included. This is a realistic number of counts for the single photon detectors that are used in this thesis.

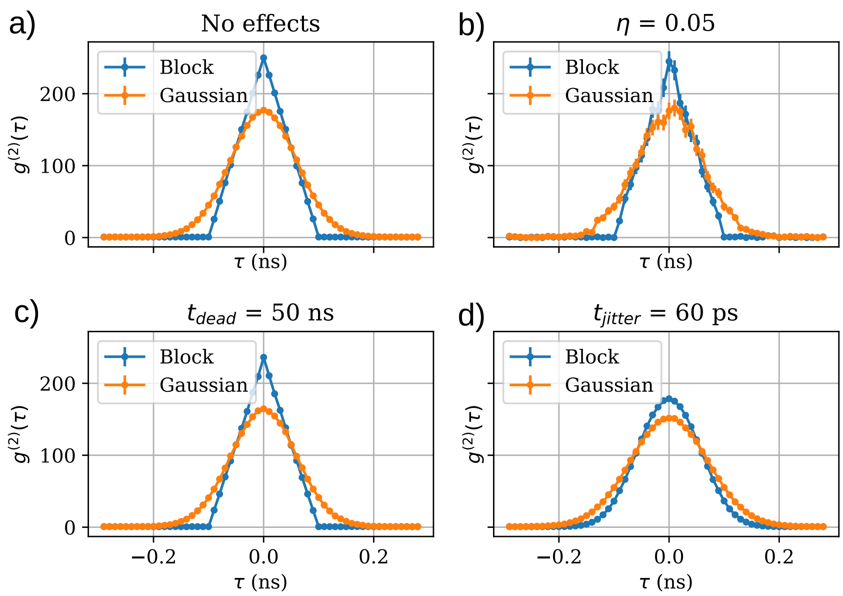

Figure 3.3: *Simulation of different detector effects for block pulses and Gaussian pulses. The pulses were simulated for* 0.5 s *with a pulse duration of* 100 ps, *a period of* 100 ns, *an intensity of* 10^{10} photons/sec *and* 0.1 % *background light.*

In Figure 3.3, only one detector effect was simulated at a time. Figure 3.3b shows that for a low quantum efficiency, less photons are detected, resulting in a more noisy signal. Other than that, the shape of $g^{(2)}(\tau)$ is not affected. In Figure 3.3c it can be seen that the peaks become a little lower when a dead time is added, indicating that photons which should have been detected in the pulse are now missed due to the dead time. This is because, without the quantum efficiency limiting the number of counts, the photon rate is of the same order as the maximum click rate of the detectors. In a normal experimental setup, the detectors should not be detecting at this dead time limit. In the simulation this was done on purpose, to visualize the effects the dead time would have if a detector is overexposed.

Figure 3.3a shows that for a perfect detector, the block pulse results in a triangular shape and the Gaussian pulse results in a Gaussian shape. Figure 3.3d shows that this measured shape changes if a timing jitter is added. The block pulse now resembles a Gaussian, and the Gaussian pulse now results in a wider peak. The timing jitter of the detectors is thus an important effect which has to be taken into account when analyzing the HBT measurements, as it has a widening effect on the measured peaks.

3.2.3 Start-stop versus full cross-correlation

The theory of Section 2.3 predicts that if $\tau \ll R^{-1}$, with R the photon click rate, then the histograms of coincidence counts for start-stop operation $K(\tau)$ and for full cross-correlation $J(\tau)$ should have the same shape. The simulations of Sections 3.2.1 and 3.2.2 used full cross-correlation, as this is the formal definition of $g^{(2)}(\tau)$. In this section, the HBT measurements of the laser pulses are also simulated with start-stop operation to compare the results of the two methods. The start-stop operation is simulated by a timer that is started when a click is registered on detector 1, and stopped when a click is registered on detector 2. Extra photons registered on detector 1 before detector 2 has clicked are ignored and do not restart the timer.

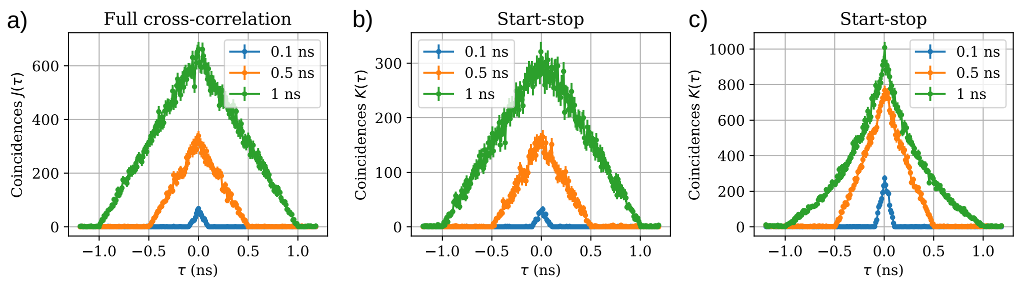

Figure 3.4: *Simulation of full cross-correlation and start-stop operation for block pulses with perfect detectors and* 0.1% *background light. The pulses were simulated with three different pulse durations and a period of* 100 ns. *The pulses of (a) and (b) were simulated for* 10 s *with an intensity of* $5 \cdot 10^7$ photons/sec, *and pulses of (c) were simulated for* 10 ms *with an intensity of* $5 \cdot 10^9$ photons/sec.

Pulses of different durations were simulated at two different powers to show the effect of the start-stop operation. Figure 3.4 shows the results of these simulations. The figure shows that for the higher power, the measurement of the long 1 ns pulse starts to change. This is because for this power, the click rate R is of the same order as the time difference τ of interest. However, the intensity needed to get this effect is so high that this will not be a problem in the experiments performed in this thesis.

Furthermore, it can be seen that the number of coincidence counts at the peak for full cross-correlation (Fig. 3.4a) and for start-stop operation (Fig. 3.4b) differ by about a factor 2. As explained in Section 3.2.1, all $g^{(2)}(\tau)$ measurements can be normalised to have the peak at 1. As long as the requirement $\tau \ll R^{-1}$ is met, start-stop operation should give the same normalised $g^{(2)}(\tau)$ as full cross-correlation.

Chapter 4

Pulse modulator characterization

In the characterization of the electro-optic modulator (EOM) there are two important quantities which should be determined. Those quantities are the pulse duration, which ideally should be shorter than 30 ps, and the extinction ratio (ER), which should be at least a factor 100. To determine those quantities, Section 4.1 explains the experimental setup. Section 4.2 discusses the stability of the EOM bias operating point. Section 4.3 explains the method that is used to fit the $g^{(2)}(\tau)$ data, and Section 4.4 presents and discusses the results. Section 4.5 shows the results of TCSPC measurements done with the trigger output of the pulser electronics. Finally, based on the results of Section 4.4, the power dependence of the EOM is tested in an additional experiment presented in Section 4.6.

4.1 Experimental setup and methods

As explained in Chapter 2, a HBT experiment can be used to measure the $g^{(2)}(\tau)$ function, which shows the intensity fluctuations of the pulsed light. Through these intensity fluctuations, information about the original pulses can be recovered. The HBT setup consists of a beam splitter and two detectors. In this thesis, the beam splitter is a fiber splitter and the detectors are single photon avalanche diodes (SPADs). The full setup is shown in Figure 4.1, where the HBT part is shown in the green block. The signals of the two SPADs are correlated by a Time-to-Digital Converter (TDC).

Directly after the continuous-wave (CW) laser, a small percentage of the light is split off via a glass window to a photodiode (PD), to keep track of fluctuations in the laser light. After this, a neutral density filter wheel, lambda/2 plate, and linear polarizer are placed to control the power and polarization of the laser light (blue block in Fig. 4.1). Polarization is important in this setup, as the $LiNbO_3$ crystals inside the EOM are naturally birefringent. For the EOM to work properly, the input light should be linearly polarized along the Z axis of the crystal. To maintain the linear polarization of the light after the polzarizer, the light is coupled to a polarization maintaining (PM) single mode fiber (SMF). This fiber then feeds the CW light to the EOM, which then outputs pulsed light into another PM SMF. The rest of the setup after the EOM is polarization insensitive, therefore regular non-PM fibers are used.

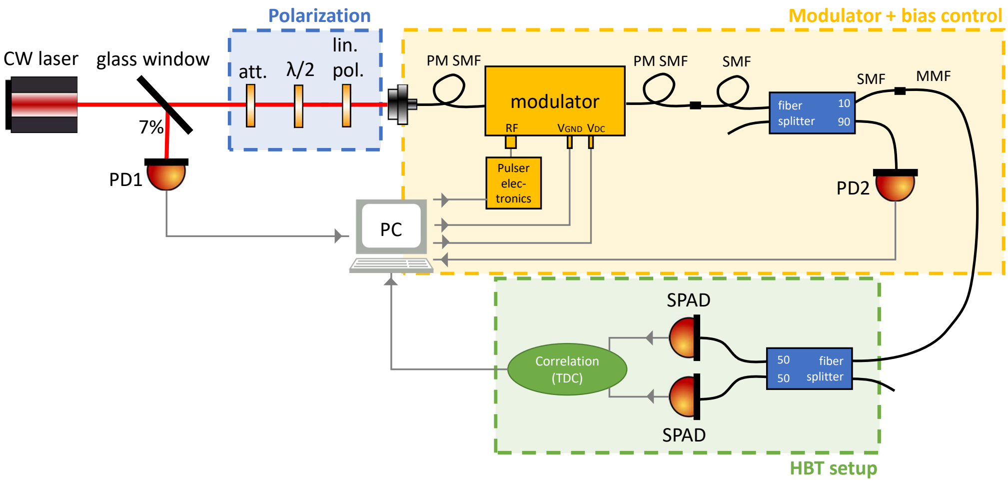

Figure 4.1: *Schematic diagram of the experimental setup used to perform the HBT measurement of the laser pulses. The blue "Polarization" block shows components used to control the intensity and polarization of the light. The yellow "Modulator + bias control" block shows the EOM, pulser electronics, and the bias control setup. Finally the green "HBT setup" block shows the HBT part of the experiment.*

Figure 4.1 also schematically shows the electronics which control the EOM (yellow block in Fig. 4.1). The RF-port is driven by the pulser electronics, which are in turn driven by the PC. The DC electrodes are connected to the analog outputs of a NI USB-6001 DAQ, which is also used to record the intensity of the output light measured with with PD2. The signal of PD2 can be used to determine the operating point of the bias V_{DC}, and automatically control the DC bias during the experiments. The bias voltage V_{DC} should be set to the half-wave voltage V_π, such that the output light is at a minimum. During experiments there can be a slight drift in V_π. In order to minimize the drift, the manufacturers of the EOM recommend to set V_{DC} to the minimum closest to $V_{DC} = 0$. To further deal with the drift, an automatic bias control program has been developed.

The laser used in the experiments is a Lion series 920-985 nm laser by Sacher Lasertechnik. The EOM is the NIR-MX950-LN-20 by iXblue. The PDs are Thorlabs PDA100A photodiodes, and the SPADs are ID Quantique ID100-MMF50 single-photon detectors. Two different TDCs are used to do the correlation; a Chronologic HPTDC8-PCI and a Becker-Hickl SPC-330. For most of the HBT experiments in this research project, the Becker-Hickl card is used, as this card has a better time resolution.

4.2 Stability of the bias operating point

The transfer function of the EOM tends to drift due to thermal changes, thermal inhomogeneity, aging, photo refractive effects and static electrical charge accumulation [12]. This drift is a slow drift compared to the measurement timescale. Measurements of this drift are shown in Section 4.2.1. Algorithms to maintain the correct operating point are presented in Section 4.2.2.

4.2.1 The modulator transfer function

The transmission of the EOM as function of the DC bias voltage was monitored during several measurement days, and during the course of this thesis, shifted a total of about 2 V. A particularly large shift happened within one week (Fig. 4.2a). During the different measurements, different behaviours could be observed. On some days, the transfer function was extremely stable (Fig. 4.2b). On other days, the transfer function drifted significantly during the experiments (Fig. 4.2c).

On the days where the transfer function was most stable, the laser power was kept constant. However, this could also be a coincidence. An experiment could be done to test if the transfer function of the EOM has a power or frequency dependence. Perhaps the environmental conditions (temperature, humidity) could also play a role. The transfer function was sometimes measured to have a smooth maximum (Fig. 4.2a,b), and other times to have a noisy maximum (Fig. 4.2c). The reason for the varying behaviour of the EOM was not addressed in this thesis. Instead, several approaches of monitoring the minimum of the EOM transfer function were tested.

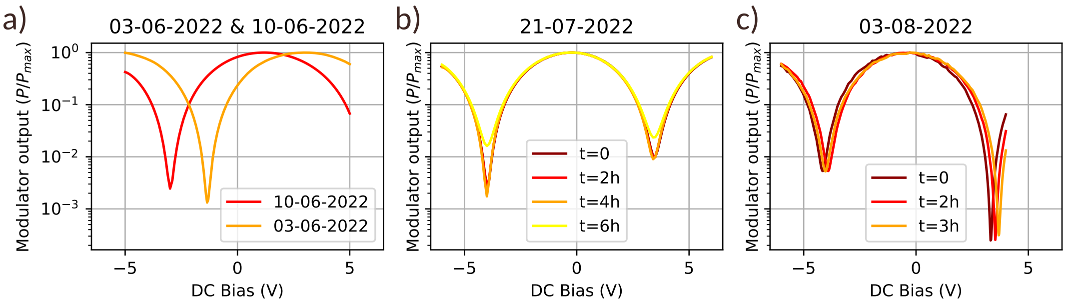

Figure 4.2: *The transfer function of the EOM, plotted in log scale, measured over the course of 2 months. Figure (a) shows a significant change of the transfer function. Figure (b) shows a day where the transfer function was extremely stable in the span of 6 hours. Figure (c) shows a day where the transfer function drifted significantly in the span of 3 hours.*

To minimize the drift, the operating point of the EOM should be set to the minimum in the transfer function that is closest to $V_{DC} = 0$. For most of the experiments shown in this thesis, this was the negative minimum. Overall, this negative minimum also appeared to be the most stable. On days where the transfer function showed a drift, it was mostly the positive minimum which drifted. The negative minimum was also measured to be lower on most days. The transfer functions of Figure 4.2 show typical extinction ratios around a factor 400 for the negative minimum. However, since the curves were measured with a simple photodiode and the minimum was close to the detection limit, this is only a rough estimation.

4.2.2 Automatic bias control algorithms

A simple automatic bias control algorithm was devised and tested in the unstable positive minimum. To provide feedback to the algorithm, the output of the EOM is measured with a photodiode, which averages over one second for each datapoint. The algorithm does 10 small DC bias steps in one direction, after which it checks if the output light measured by the photodiode got higher or lower. If the output got higher, the step direction changes. If the output got lower, the step direction remains the same. This algorithm works well if the step size and averaging are large enough to be above the noise. However, it slightly lowers the average extinction ratio, as the algorithm continuously steps out of the minimum. Because of this, and the general stability of the negative minimum, it was chosen to manually monitor the operating point for most of the measurements presented in Chapter 4 and all the cQED measurements of Chapter 5.

For future applications it would be preferable to design a second bias control algorithm for these stable minima. Such an algorithm would require extremely slow updates, on the scale of minutes. If the algorithm takes small steps out of the minimum, the operating point will not be optimal. To minimize the hindrance of this to the experiment, these steps should not last long. The algorithm should also only take steps if a drift of the minimum is observed, to prevent unnecessary hindrance of the experiment. An example of an algorithm would be to monitor the output of the EOM and average it into one data point per minute. As soon as one of these measurements deviates a certain percentage from the previously achieved minimum, the algorithm should take steps to find the new minimum. These steps should consist of two quick, small steps of 1 second into both bias directions. If one of these steps results in a lower power, more steps in that direction should be taken to find the new minimum. After this, the bias should again be kept constant until a data point is recorded which deviates too much from the minimum.

4.3 Fitting models

The goal of the experiments is to extract the pulse duration and extinction ratio of the generated pulses, and ideally say something about the shape of the pulses. In order to do this, good understanding of the $g^{(2)}(\tau)$ function is required. An accurate model for $g^{(2)}(\tau)$ is based on two convolutions, which involve a pulse ansatz and the detector response function. The first step in fitting the data is thus obtaining the detector response function, which is done in Section 4.3.1. After this, the data can be fitted with a model consisting of the pulse ansatz and numerical convolutions, which is explained in Section 4.3.2. The pulse duration can be directly fitted as parameter, but extracting the extinction ratio from the $g^{(2)}(\tau)$ data is more difficult. The method to estimate the extinction ratio is explained in Section 4.3.3.

4.3.1 SPAD Detector response

For the $g^{(2)}(\tau)$ model to be accurate, it is important to know the detector response function. The response of a single photon avalanche diode (SPAD) typically consists of a Gaussian with an exponential diffusion tail [18–20]. The FWHM of the Gaussian is defined as the timing jitter of the detector. For estimation purposes the detector response can often be assumed to be a Gaussian, but for the model in this thesis the exponential tail is included to achieve an accurate fit. To be able to calculate the convolutions of the model, a function of this detector response is needed. Such a function can be obtained by using a model or by interpolation. Both methods require experimental data of the detector response, which can be obtained with a Time-Correlated Single Photon Counting (TCSPC) measurement. TCSPC is a technique which measures arrival times of photons in respect to a reference signal provided by the light source. If the light source is a pulsed laser with sufficiently short pulses (<1 ps), and the pulses are directly measured by the detector, the result of the TCSPC measurement will be the detector response function.

The SPADs used in the HBT measurements of the laser pulses are ID100-MMF50 single-photon detectors, which according to their specifications have a jitter of 40 ps. The specifications also show the response function of the detectors, which can be extracted from the datasheet by using a data-extracting tool. Upon further inspection of the extracted data, the jitter appears to be 66 ps. We also performed our own TCSPC measurement, which shows a jitter of 60 ps. Both the datasheet response and the measured reponse are shown in Figure 4.3. In this figure, a small offset of 0.004 was added to the datasheet curve to match the slopes of the diffusion tails. The TCSPC measurements showed no change in detector response if the power of the light incident on the detectors was varied. The measured response will be used as detector response function in the model.

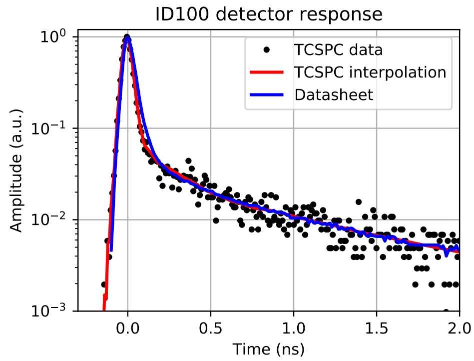

Figure 4.3: *Interpolations of the timing response of the ID100 SPADs. The y-axis shows normalized counts on a log scale and the x-axis time in ns, where the peaks are shifted to t=0. The blue line the extracted data from the ID100 datasheet and the red line shows the TCSPC measurement interpolation.*

4.3.2 A numerical model for the HBT measurements

The $g^{(2)}(\tau)$ data is fitted with a numerical model. The model assumes a pulse shape $P_{pulse}(t)$, and first generates this shape using the pulse duration t_{fwhm} as parameter for the FWHM of the pulse. Assumed pulse shapes in this thesis are Gaussian pulses and block pulses. The time discretization is chosen a factor 100 smaller than the time resolution of the data. The detector response function $P_{det}(t)$ is sampled with the same time discretization. We then obtain $g^{(2)}(t)$ by the following calculation:

$$g^{(2)}(t) = \Big(P_{pulse}(t) * P_{det}(t)\Big) \star \Big(P_{pulse}(t) * P_{det}(t)\Big) \tag{4.1}$$

Note that cross-correlation ($\star$) is the same as convolution ($*$) with the reversed function ($t \rightarrow -t$). Due to the commutative and associative properties of the convolution operation, this can also be written as:

$$\begin{aligned} g^{(2)}(t) &= \Big(P_{pulse}(t) \star P_{pulse}(t)\Big) * \Big(P_{det}(t) \star P_{det}(t)\Big) &(4.2)\\ &= g^{(2)}_{pulse}(t) * g^{(2)}_{det}(t) &(4.3)\end{aligned}$$

In other words, $g^{(2)}(t)$ is the convolution of the perfect non-jitter-limited $g^{(2)}_{pulse}(t)$, and the detector response $g^{(2)}_{det}(t)$. The model performs the convolutions in this order, and scales $g^{(2)}_{pulse}(t)$ to have height A and offset b. This allows a calculation of the extinction ratio using the derivation in Section 4.3.3. The resulting shape is then given the correct position τ_0 for the fit. This numerically calculated $g^{(2)}(\tau)$ is then interpolated, after which the interpolation is sampled at the desired points. This model thus fits the duration of the original pulse t_{fwhm}, the non-jitter-limited $g^{(2)}(\tau)_{pulse}$ peak height A and offset b, and the position of the peak τ_0.

4.3.3 Estimating the extinction ratio

The extinction ratio is the ratio between the light at the pulse peaks and the background light. Naively one would think the extinction ratio can then be easily extracted from the peak-to-background ratio of the $g^{(2)}(\tau)$ data. However, this ratio of the $g^{(2)}(\tau)$ data depends on the pulse shape, pulse width and repetition rate of the pulses. To calculate how to convert the peak-to-background ratio to the original extinction ratio, we assume the pulse signal $I(t)$ consists of a periodic pulse signal $I_p(t)$ and a constant background I_{bg}:

$$I(t) = I_p(t) + I_{bg} \tag{4.4}$$

The pulse signal $I_p(t)$ has an intensity of I_{peak} at the peak, as is shown in Figure 4.4. Since we are interested in the ratio between peak and background, and the denominator of $g^{(2)}(\tau)$ (Eq. 2.3) is constant, we only need to evaluate the numerator:

$$\begin{aligned} g^{(2)}(\tau) &\sim \langle I(t)I(t+\tau)\rangle && (4.5)\\ &= \big\langle \big(I_p(t)+I_{bg}\big)\big(I_p(t+\tau)+I_{bg}\big)\big\rangle && (4.6)\\ &= \big\langle I_p(t)I_p(t+\tau)\big\rangle + 2I_{bg}\langle I_p\rangle + I_{bg}^2 && (4.7) \end{aligned}$$

Since the background light I_{bg} is constant and time-independent, it can be taken outside of the angled brackets, which indicate a time average. The last step to Eq. 4.7 also uses the fact that the time average of I_p is constant, $\langle I_p(t)\rangle = \langle I_p(t+\tau)\rangle = \langle I_p\rangle$. The value of the peak in $g^{(2)}(\tau)$, which will be referred to as A (see Fig. 4.4), is found at $\tau = 0$. For $\tau = 0$, we can write $\big\langle I_p(t)I_p(t+\tau)\big\rangle = \langle I_p^2\rangle$, which is the time average of the pulse signal squared. The value of the background in $g^{(2)}(\tau)$, which will be referred to as b, is given for some τ for which the peaks of $I_p(t)$ and $I_p(t+\tau)$ have zero overlap. There, $\big\langle I_p(t)I_p(t+\tau)\big\rangle = 0$. This means that the relations between the peak A and background b in $g^{(2)}(\tau)$ and the original signal $I_p(t)$ with background I_{bg} are given by:

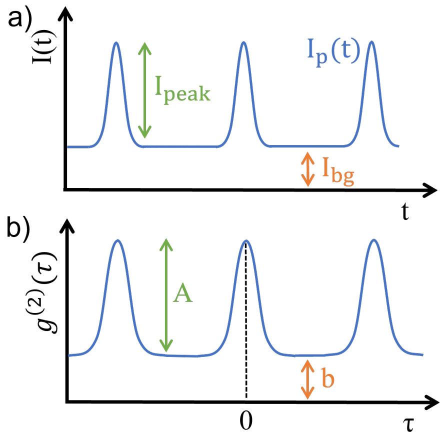

Figure 4.4: *Drawing showing the definitions of the different parameters in (a) time domain and (b) $g^{(2)}(\tau)$.*

$$A = \langle I_p^2\rangle, \quad b = 2I_{bg}\langle I_p\rangle + I_{bg}^2 \tag{4.8}$$

Here the relation for b can be solved for I_{bg} to obtain:

$$I_{bg} = -\langle I_p\rangle + \sqrt{\langle I_p\rangle^2 + b} \tag{4.9}$$

The last step then consists of assuming a pulse shape and writing $\langle I_p\rangle$ and $\langle I_p^2\rangle$ in terms of I_{peak}. The pulses are assumed to have a duration t_{fwhm} and period T. For a block pulse it can then be shown that:

$$\langle I_p\rangle = I_{peak}\frac{t_{fwhm}}{T}, \quad \langle I_p^2\rangle = I_{peak}^2\frac{t_{fwhm}}{T} \tag{4.10}$$

For a Gaussian pulse with standard deviation $\sigma \approx t_{fwhm}/2.355$ it can be shown that:

$$\langle I_p \rangle = I_{peak}\sqrt{2\pi}\frac{\sigma}{T}, \quad \langle I_p^2 \rangle = I_{peak}^2\sqrt{\pi}\frac{\sigma}{T} \tag{4.11}$$

To make the equations more clear, they can be written in terms of the duty cycle D. The duty cycle represents the fraction of one period in which the pulse is on. For the Gaussian pulse this is $D_g = \sqrt{2\pi}\frac{\sigma}{T}$ and for the block pulse this is $D_b = \frac{t_{fwhm}}{T}$. The following expressions for the extinction ratios can then be derived, using equations 4.8, 4.9, 4.10 and 4.11:

$$ER = \frac{I_{peak} + I_{bg}}{I_{bg}} \tag{4.12}$$

$$ER_{block} = \frac{1 - D_b + \sqrt{D_b^2 + D_b\frac{b}{A}}}{-D_b + \sqrt{D_b^2 + D_b\frac{b}{A}}} \tag{4.13}$$

$$ER_{Gauss} = \frac{1 - D_g + \sqrt{D_g^2 + \frac{D_g}{\sqrt{2}}\frac{b}{A}}}{-D_g + \sqrt{D_g^2 + \frac{D_g}{\sqrt{2}}\frac{b}{A}}} \tag{4.14}$$

This derivation makes the assumption that the intensity is the same on both detectors. It is also assumed that the measurement is not affected by detector jitter. In the actual experiments performed in this thesis, this assumption does not hold. However, the model as presented in Section 4.3.2 circumvents this problem by directly fitting A and b.

4.4 Second-order correlation function results

The results of the HBT measurements done to characterize the pulse modulator are presented and discussed in this section. First we show the measured $g^{(2)}(\tau)$ shapes and the fitted curves in Section 4.4.1. Then, in Section 4.4.2, we present the fitted pulse durations, and in Section 4.4.3 we present the calculated extinction ratios. Further implications of the results for single photon generation will be discussed in Chapter 5.

4.4.1 Pulse shape for short versus long pulses

Figure 4.5 shows the measured $g^{(2)}(\tau)$ data and fits for two different pulses. For one pulse (delay1, delay2) = (0 ps, 0 ps), and for the other the delays were (0 ps, 500 ps). Multiple settings for the delays were tried, and the pulses could be observed to disappear into the background at (70 ps, 0 ps). From that point, increasing the difference delay2-delay1 increases the pulse duration. The (0 ps, 0 ps) pulse is a short pulse of estimated duration 68 ± 1 ps. The (0 ps, 500 ps) pulse is a long pulse of estimated duration 391 ± 4 ps. For these estimations, a Gaussian pulse ansatz was used.

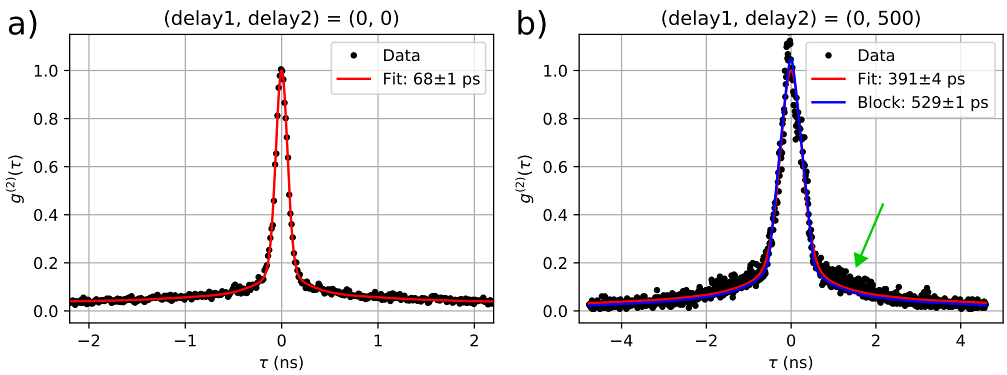

Figure 4.5: *Measured $g^{(2)}(\tau)$ for (a) a pulse with (delay1, delay2) = (0 ps, 0 ps) and (b) a pulse with (delay1, delay2) = (0 ps, 500 ps). The red lines show fits to the data assuming a Gaussian pulse. The blue line in (b) shows a fit assuming a block pulse.*

As can be seen in the figure, the fit matches the data for the short pulse quite well. For the long pulse there appears to be a slight deviation (green arrow). For longer pulses one might expect a block pulse instead of the assumed Gaussian pulse. A fit with a block pulse ansatz is shown in Figure 4.5 in blue. It can be seen that this does not explain the deviation. The differences between Gaussian and block pulse shapes in the $g^{(2)}(\tau)$ measurement can be studied with the model. For short pulses, both pulse shapes give the same result, as this regime is heavily limited by the detector response. Therefore, for short pulses the pulse shape can not be recovered from $g^{(2)}(\tau)$. For the longer pulses, the block pulse results in a more triangular $g^{(2)}(\tau)$ shape. This is illustrated in Figure 4.6, and mainly results in a difference in $g^{(2)}(\tau)$ width for the two pulse shapes. This explains why the block pulse fit in Figure 4.5 obtains a pulse duration of 529 ± 1 ps.

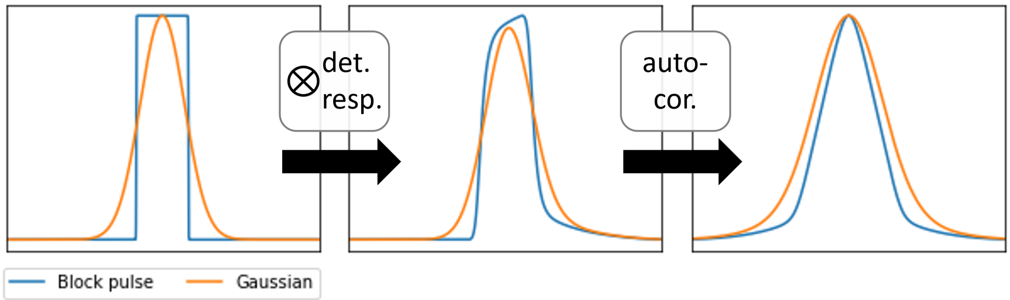

Figure 4.6: *The difference in the model between a Gaussian (orange line) and block pulse (blue line) assumption, for long pulses. Shown is the original pulse, the convolution with detector response, and the autocorrelation. Both original pulses have a FWHM of 500 ps. The time axes of the three figures are equal.*

The slight deviations from the fit in Figure 4.5b increase with the duration of the pulse. These deviations could be caused by the EOM not immediately fully returning to the operating point V_π after the long pulse. However, from this data, a clear origin of the deviations can not be concluded. This data also gives no conclusion on the shape of the long pulses, although the block pulse seems to be a slightly better fit at the peak. Section 4.5 will present TCSPC measurements using a trigger output of the EOM. These TCSPC measurements allow further discussion on the shape of the pulses.

4.4.2 Pulse duration

The original durations of the pulses can be reconstructed from the fits. The results of these reconstructions are shown in Figure 4.7. This figure shows data that was measured on four different days, using the negative DC bias minimum of the EOM. See Appendix I for additional data which was measured in the noisy positive minimum. Between those days, the laser power slightly varied due to different attenuation and coupling into the fiber. The figure shows two linear fits; $y = (0.64 \pm 0.02)x + (74 \pm 2)$ ps for the model assuming a Gaussian pulse, and $y = (0.81 \pm 0.02)x + (109 \pm 5)$ ps for the model assuming a block pulse. In reality the short pulses can be expected to be Gaussian and the long pulses can be expected to be more block-shaped. The actual relation might thus be something in between the two fits.

It should be noted that the reconstructed pulse duration heavily depends on the detector jitter assumption. Assuming a Gaussian detector

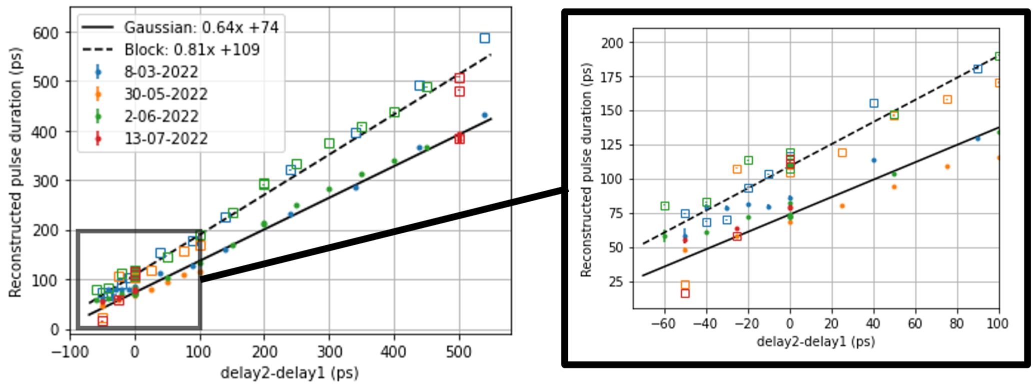

Figure 4.7: *The reconstructed pulse durations for Gaussian pulse assumptions (circles) and block pulse assumptions (squares). The colors indicate data taken at different days. The solid black line indicates a linear fit through the Gaussian-ansatz data, and the dashed black line indicates a linear fit through the block-ansatz data. The figure on the right shows a zoomed-in plot of the short pulse region.*

jitter t_{jit} and Gaussian pulse with duration t_{fwhm}, the relation between the jitter and reconstructed pulse duration is:

$$\Delta\tau = \sqrt{2}\sqrt{t_{jit}^2 + t_{fwhm}^2} \quad \Longrightarrow \quad t_{fwhm} = \sqrt{\frac{\Delta\tau^2}{2} - t_{jit}^2} \tag{4.15}$$

Here $\Delta\tau$ is the FWHM of the measured $g^{(2)}(\tau)$ peak. This relation shows that the jitter affects shorter pulses more than longer pulses. This means that if the actual jitter were to differ, the slope of the linear fit in Figure 4.7 would also differ. From the way the electronics generate the pulses, one would expect the pulse duration to increase on a 1:1 ratio with the difference between delay1 and delay2. This would mean the slope of the linear fit should be 1. Even with a linear fit starting at the Gaussian pulses and ending at the block pulses, this data does not produce a slope of 1. This could indicate that the assumed detector response is too narrow. This means the reconstructed pulse durations are likely overestimates, and the actual pulse durations are shorter.

In data measured with the trigger output of the EOM (Sec. 4.5), the pulses could still be observed at (delay1, delay2) = (75 ps, 0 ps). By extrapolating the linear fits of Figure 4.7 to this setting, we can find an estimate for the shortest pulses that should be possible, assuming the relation remains linear in the short-pulse regime. The Gaussian ansatz gives a pulse duration of 26 ± 3 ps and the block pulse ansatz gives a duration of 48 ± 5 ps. It is reasonable to assume that the shortest pulses have a Gaussian shape. Due to the uncertainties caused by the detector response and pulse shape it is difficult to conclude a definite shortest pulse duration, but based on Figure 4.7 it may be concluded that the shortest pulses are of the order of ~ 50 ps. Due to the large time span between the different measurements of Figure 4.7 (months), it can also be concluded that the pulse modulator is stable over time.

4.4.3 Pulse extinction ratio

An important characteristic for the performance of the EOM is the extinction ratio (ER) that can be achieved. The extinction ratio can be calculated from the parameters which are fitted by the model, using Equation 4.14. Since the results for block and Gaussian shapes are similar, the choice is made to assume Gaussian pulses in this section. The calculated extinction ratios are shown in Figure 4.8, and show extinction ratios up to almost 30 dB. The figure also includes data from the TCSPC measurements (Sec. 4.5), respresented as crosses. The color of the plotted points shows a measure of the intensity at the peaks of the pulses. For the TCSPC measurements this intensity can be directly determined as:

$$I_{peak}^{trig} = \frac{T_{trig}}{T_{pulse}} \frac{A+b}{b} \tag{4.16}$$

.

Here A and b are the fitted non-jitter-limited peak and background, and T_{trig}, T_{pulse} are the periods of the trigger and pulses. The factor $\frac{T_{trig}}{T_{pulse}}$ accounts for different trigger rates used. For the HBT measurements, this intensity value is estimated with:

$$I_{peak}^{HBT} = C\tilde{I}_{peak}^{HBT} = C\sqrt{\frac{A}{D_g}} \tag{4.17}$$

This expression is based on Equation 4.11. The constant C brings the trigger and HBT measurements to the same scale, and is calculated by comparing the calculated $\tilde{I}_{peak}^{HBT}$ and I_{peak}^{trig} for measurements where the optical power was equal. C was determined to be ~ 750. The measurements used for the estimation of C are the high-ER measurements of values below a delay difference of 0. It can be seen that the reconstructed extinction ratios for these HBT and TCSPC measurements of equal optical power were similar.

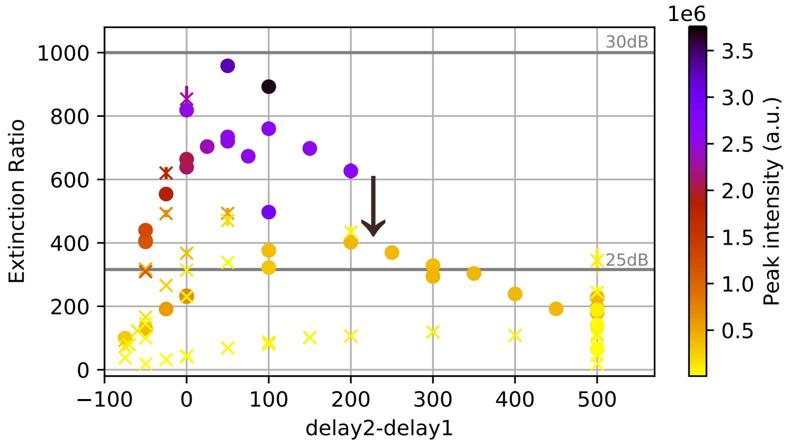

Figure 4.8: *The reconstructed extinction ratios for different pulse durations and different laser powers. The color indicates an estimate of the intensity at the peaks of the pulses. The dots represent HBT measurements and the crosses TCSPC measurements (Sec. 4.5). The arrow indicates a decrease of a factor* ~ 10 *in optical power.*

Figure 4.8 shows a clear power dependence of the reconstructed extinction ratio. In all measurements, the laser power was varied in front of the EOM, as indicated in Figure 4.1. The two measurements indicated by the arrow (delay2-delay1 = 200) were taken sequentially, where the laser power was lowered by a factor 10 in between. To find out if the power dependence is caused by the EOM or by the detectors, additional measurements were done. The results of these measurements and further conclusions about the power dependence of the EOM are presented in Section 4.6.

Figure 4.8 also shows that for delay differences below 0 the pulses start to collapse, completely disappearing at delay2-delay1 = -80 ps. This agrees with earlier measurements done by the ELD with a spectrum analyzer, which found that the electrical pulses disappear at a delay difference of -80 ps. Furthermore, the ELD found that for a delay difference of -65 ps the pulses were already collapsing, with an estimated FWHM of 40 ps.

Finally, Figure 4.8 shows extinction ratios up to 30 dB, with most of the points exceeding the typical 25 dB provided by the specifications of the EOM. The specifications do not mention a maximal extinction ratio, but do show a figure where a static extinction ratio of $\sim$ 32 dB is achieved. The high extinction ratios shown in Figure 4.8 thus agree with the specifications of the EOM. Since the amplitude of the electrical pulses is likely not yet optimal, an additional experiment can be done to increase the extinction ratio. If the amplitude of the electrical pulses can be varied, the extinction ratio can be measured as function of electrical pulse height. The electronics do currently have a parameter which should slightly vary the amplitude of the pulses (V_R), but this parameter also likely slightly varies the durations of the pulses, so it was chosen to keep this value constant in the experiments done in this thesis.

In the measurements of Figure 4.8, the pulse repetition frequency for most points was 50 MHz. Measurements which had a slightly different repetition frequency (10 MHz - 50 MHz) did not deviate from the other measurements. A dependence of the extinction ratio on the wavelength of the laser light was not investigated, but could be present.

4.5 Triggered TCSPC

The fast pulser electronics developed by the ELD also have a trigger output. This trigger is derived from the same clock that generates the electrical pulses and can be used for Time-Correlated Single Photon Counting (TCSPC) measurements. TCSPC is a technique which measures arrival times of photons in respect to a trigger signal. This can for example be used to do time-resolved resonant fluorescence spectroscopy, to measure the lifetime of a quantum dot. The trigger output can also be used for synchronization purposes such as heralding events.

In this section, the trigger output is used to do TCSPC with the optical pulses generated with the EOM. In order to do this, one of the detectors in the measurement setup is replaced by the trigger signal. The result of the measurement will then be the convolution of the original pulse with the detector response. This measurement can thus be deconvoluted with the detector response to reconstruct the shape of the original pulse. However, to extract the duration and extinction ratio of the pulses, it is easier to assume a Gaussian pulse and directly fit the convolution to the measured data. The results of this are presented in Section 4.5.1, followed by a discussion on pulse shape reconstruction by deconvolution in Section 4.5.2.

4.5.1 Pulse duration and trigger jitter

To measure a TCSPC curve, the period of the trigger should be an integer multiple of the period of the pulses. Different repetition rates for the trigger were tested (1 MHz, 12.5 MHz, 25 MHz), for a pulse repetition rate of 50 MHz. The results show no dependence on the trigger rate, so this will further be ignored in this section. The reconstructed extinction ratios were already shown in Section 4.3.3, and matched the HBT measurements well. The reconstructed pulse durations are shown in Figure 4.9.

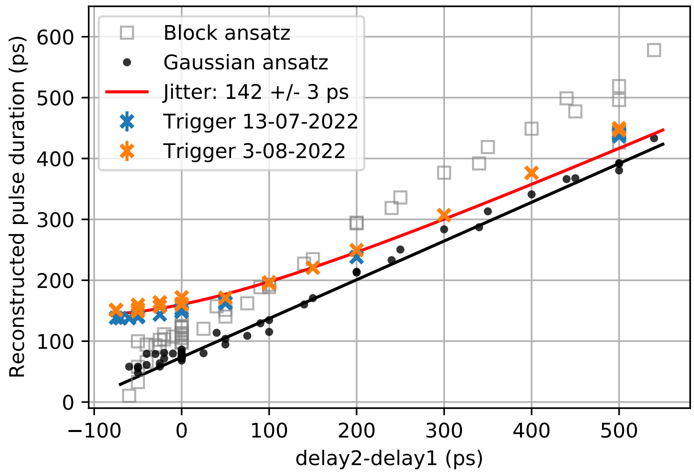

Figure 4.9: *Reconstructed pulse durations for the TCSPC measurements. The black dots and grey squares show the results of the HBT measurements (Sec. 4.4.2) for a Gaussian and block pulse ansatz respectively. The red line through the trigger data shows a fit where a Gaussian jitter of 142 ps was added to the fit of the black line.*

The reconstructed pulse durations for the TCSPC measurements are consistently longer than the pulse durations reconstructed from the HBT measurements, and appear to plateau for short delay differences. Since the setup used the same measurement equipment, this indicates that there is a jitter in the trigger signal. If the trigger pulses have a significant temporal uncertainty, the measured response will widen. For a simple estimation of this jitter, we can assume the original pulse, detector response, and trigger jitter are all Gaussian. The measured width of the TCSPC peak Δt_{meas} is then given by:

$$\Delta t_{meas} = \sqrt{t_{fwhm}^2 + t_{det}^2 + t_{jitter}^2} \tag{4.18}$$

Here t_{fwhm} is the duration of the pulse, t_{det} is the FWHM of the detector response and t_{jitter} is the jitter of the trigger. The jitter can thus be added to the linear fit $ax + c$ through the following equation:

$$t_{reconstructed} = \sqrt{(ax + c)^2 + t_{jitter}^2} \tag{4.19}$$

Here x is the delay difference delay2-delay1. Equation 4.19 is fitted to the data, see Fig. 4.9, and fits a jitter of 142 ± 3 ps. This low uncertainty follows from the fit, but in reality this is a rough estimate due to the assumptions made. It can be concluded that the trigger likely has a jitter of order 140 ps. Possible elements of the electronics which can cause this jitter are the voltage controlled oscillator (VCO) and the slow CMOS-output of the FPGA. It is unlikely that the jitter originates from the VCO, since the jitter would then propagate also to the optical pulses, which has not been observed. This leaves the CMOS-output as likely culprit. In this case, a solution could be to use a different type output of the FPGA. A more detailed schematic of this part of the electronics is given in Appendix II.

4.5.2 Reconstructing the pulse shape

The HBT measurements can not be deconvoluted, since deconvolution of two shapes requires knowing one of the two shapes, and the measured peak is an autocorrelation. With TCSPC, the measured peaks can be deconvoluted, because this includes only a single convolution and the detector response is known. Because the data is noisy, a Wiener deconvolution is used. This is a deconvolution which is performed in the frequency domain, to minimize the impact of deconvolved noise.

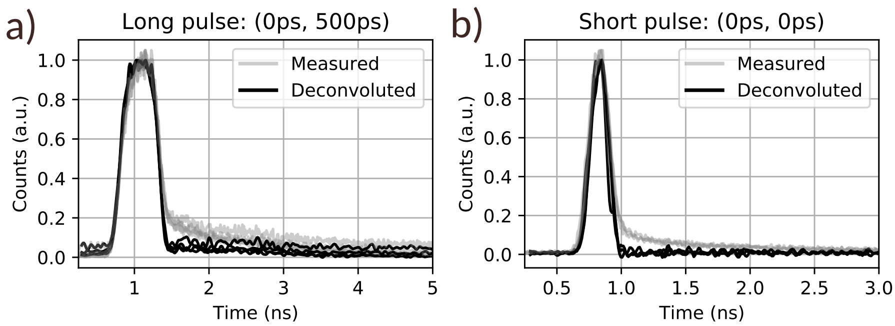

Figure 4.10: *Deconvoluted TCSPC measurements. The grey lines show the original measurements and the black lines the deconvolutions with the detector response. Figure (a) shows a long pulse of* $\sim$ 520 ps *and (b) a shorter pulse of* $\sim$ 160 ps.

The results of the deconvolution are shown in Figure 4.10. This figure shows that the longer (0 ps, 500 ps) pulse indeed appears to be a block pulse, and the shorter (0 ps, 0 ps) pulse a Gaussian pulse. The TCSPC measurement was deconvoluted with only the detector response, so the shapes of Figure 4.10 still include the convolution of the $\sim$ 140 ps jitter. The widths of these deconvoluted peaks, through quick estimation by hand, are $\sim$ 520 ps and $\sim$ 160 ps. The widths fitted with the Gaussian ansatz in Figure 4.9 for these pulses were 440 ps and 150 ps. The 80 ps difference for the long pulse can be explained by the different shape. It can thus be concluded that the longer pulses converge to a block-like shape, while the shorter pulses appear to be Gaussian.

4.6 Power dependence of the EOM

Section 4.4.3 indicated that the extinction ratio might be power dependent. In this section, an experiment is performed to investigate this power dependence. The setup is adjusted so that the power can be varied both in front of and after the EOM. This way, the power on the detectors can be kept constant while the power through the EOM is varied, and vice versa. Figure 4.11 shows two bias sweeps taken at the start and towards the end of the experiment. The negative minimum at -3.3 V was selected as operating point, and the automatic bias control algorithm of Section 4.2.2 was used to maintain this operating point.

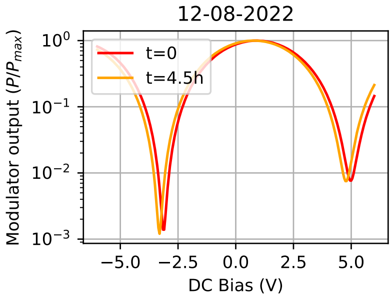

Figure 4.11: *DC bias sweeps of EOM during power dependence measurements.*

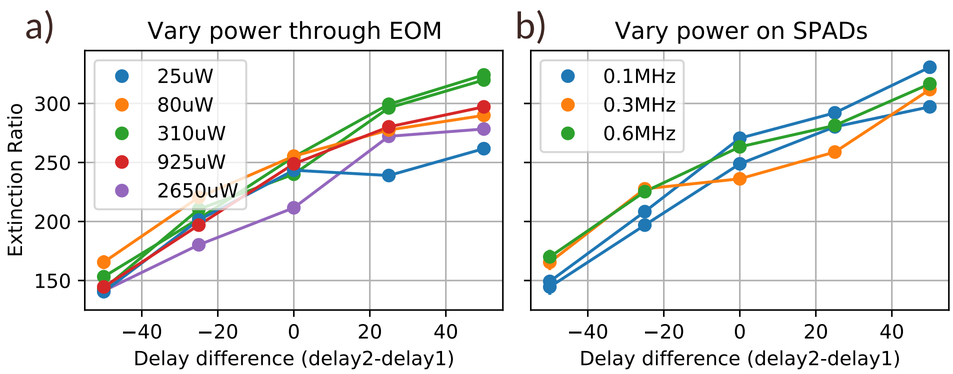

Figure 4.12: *Reconstructed extinction ratios for different pulse durations. Figure (a) shows the extinction ratios for various different powers through the EOM (detector count rate* 0.1 MHz*), and (b) shows the extinction ratios for various powers on the detectors (EOM power* 925 μW*).*

The input power through the EOM was varied between 25 μW and 2.65 mW. The power on the SPADs and clicks counted by the TDC were kept low, at around 0.1 MHz, to rule out card and detector effects. Since only short pulses are measured for the results presented in this section, a Gaussian pulse assumption is used to fit the data. The reconstructed extinction ratios are shown in Figure 4.12. Here, a power dependence could not be reproduced. The measurements seem to be independent of the power through the EOM and the power on the SPADs. To further investigate the cause for the apparent power dependence of Figure 4.8, more research is needed.

A difference between this experiment and the one shown in Figure 4.8 is the DC voltage bias minimum that was used. The previous experiment was performed on 03-08-2022 and used the positive minimum shown in Figure 4.2c. The experiment presented here was performed on 12-08-2022 and used the negative minimum shown in Figure 4.11. It could be that the positive minimum behaves differently from the negative minimum, which was generally observed to be more stable. Due to the change of the EOM transfer function over time, the bias sweeps of the two experiments look very different. This difference could also explain the difference in extinction ratios that were reached. Figure 4.12 shows extinction ratios up to 300, while the results presented in Figure 4.8 showed extinction ratios up to 1000. More research could be done to investigate the stability of the achievable extinction ratio over long time periods.

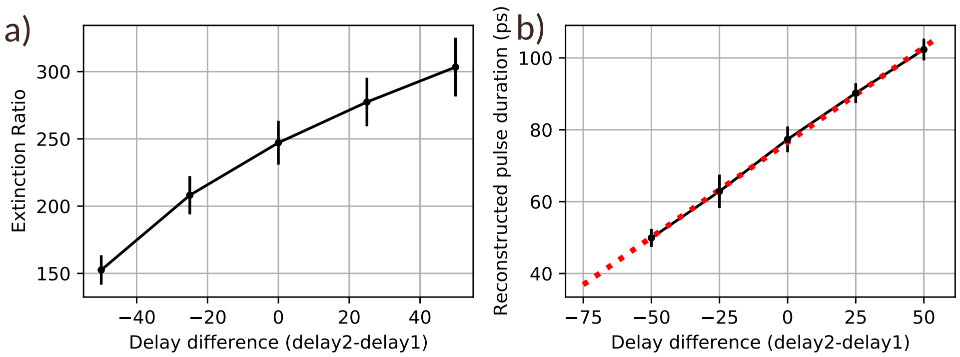

Figure 4.13: *(a) Averaged extinction ratio and (b) reconstructed pulse duration as function of delay difference. The red dotted line shows a linear fit of* $(0.53 \pm 0.01)x + (76.5 \pm 0.3)$ps.

The fits performed to reconstruct the extinction ratios of Figure 4.12 also automatically produce more data on the pulse durations. Since both the extinction ratios and pulse durations show no power dependence, all data points can be averaged to obtain a mean value and standard deviation for each point. The results of this are shown in Figure 4.13. Figure 4.13a shows that the extinction ratio is not a linear function of the delay difference, but instead is slightly curved. This can be explained by a nonlinear rise time of the electronics. The rise time determines the collapse of the pulse, as the electrical pulses stop reaching their maximum height when the pulse duration is shorter than the rise time. Figure 4.13b shows that the reconstructed pulse duration is a linear function of the delay difference, where a curve of $(0.53 \pm 0.01)x + (76.5 \pm 0.3)$ps can be fitted to the data. This curve is slightly different from the $(0.64 \pm 0.02)x + (74 \pm 2)$ that was fitted in Section 4.4.2. The difference can be explained by the absence of longer pulses in this data, which dominated the fit of Section 4.4.2. Extrapolating the linear fit to the settings for which the shortest pulses can be measured ((delay1, delay2) = (75, 0)) produces a shortest pulse duration of 37 ± 1 ps.

Chapter 5

Single-photon source experiments

In Chapter 4, the EOM was characterized to have high extinction ratios of typically 25 dB and up to 30 dB, and tunable pulse durations down to 50 ps. In this chapter, the pulses created by the EOM are used to generate single photons on demand. In order to do this, we first select a bright single quantum dot (QD) in Section 5.1, and address it with a continuous-wave (CW) laser light to verify its single photon emission character in Section 5.2. Finally, in Section 5.3, we present and discuss the results of EOM pulsed excitation of the QD in the context of single photon purity for various pulse durations.

5.1 Selection of the quantum dot

We use an InAs/GaAs microcavity-QD device which we don't describe here, see [21] for details. The cavity device used in this thesis has a shape and strain induced birefringence which results in a frequency splitting between two linear orthogonal polarization modes of the fundamental mode. We unify the reference polarization frame with the cavity polarization-splitted modes. In this reference frame, the horizontal H (vertical V) cavity mode transmits H- (V-) polarized light. The polarization-splitted cavity modes can be easily revealed by scanning the laser frequency (not shown, for reference we recommend [5, 21–23]).

To reveal and select a QD to use as single photon source, we apply a gate voltage V_G along the Z-direction of the device. This allows tuning the quantum dot exciton transition into resonance with the optical cavity mode by the quantum-confined Stark effect. This situation is presented in Figure 5.1, where we excite the structure with V-polarized light, i.e. the polarization aligned to the V cavity mode represented as white dashed line. Because the reflected laser light exceeds the emission intensity of the QD by several orders, the presented voltage scan is measured in a cross-polarization scheme, where the V polarized laser light reflected from the sample is filtered out by a linear polarizer. Due to this detection scheme, we mostly observe light originating from the QD. A good QD appears as a bright line, as can be seen in Figure 5.1, fitted by the solid black line.

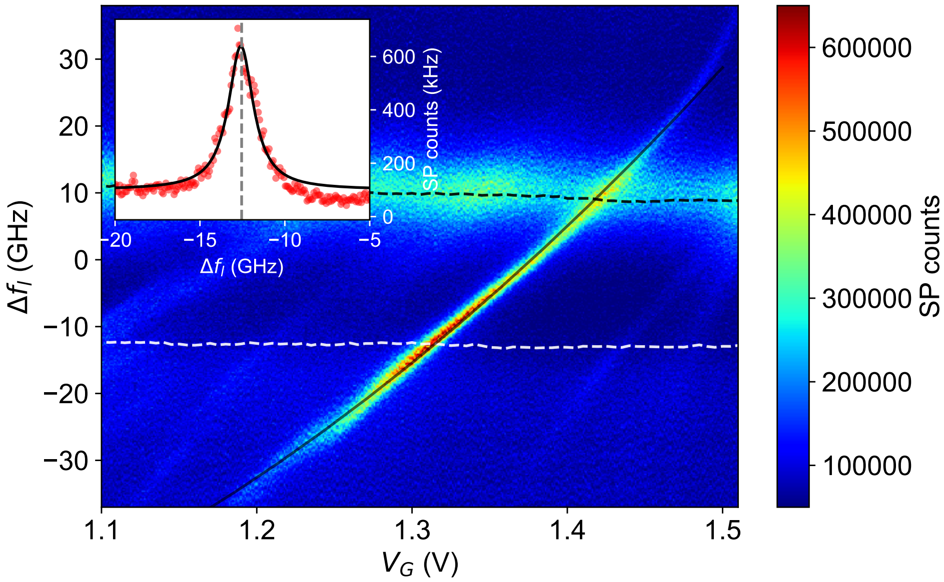

Figure 5.1: *Voltage scan of a single quantum dot, measured in cross-polarization. The H- and V-modes are determined by Lorentzian fits of scans in co-polarization and are indicated here with a black and white dashed line, respectively. The inset shows a cross-section of the scan for a voltage of 1.31 V.*

For our experiments, we choose the operation point where the QD is in resonance with the V cavity mode. This is the point in Figure 5.1 at $V_G = 1.31$ V and a laser frequency corresponding to ~ -12 GHz. Here, the QD emission is Purcell enhanced and therefore the brightest. Note that Figure 5.1 also shows emission or scattering from a contamination of the H cavity mode. However, since this is separated more than 22 GHz spectrally from our chosen point of operation, this will not be an issue for the generated single photon stream. The lifetime of the QD can be estimated from the width of the resonance peak [24]. For this QD, the width extracted from Figure 5.1 by Lorentzian fit is $\Gamma = 1.8 \pm 0.1$ GHz. This gives an estimated lifetime of $\tau_r = 1/\Gamma = 560 \pm 30$ ps.

5.2 Continuous-wave single photon correlations

To verify the single-photon character of the QD emission, we measure the second-order correlation function $g^{(2)}(\tau)$ under resonant CW excitation. Due to the quantum nature of single photon light, a dip around $g^{(2)}(0)$ is expected. The width and measured depth of this dip depend on the lifetime of the QD, the jitter of the detectors, and the single-photon purity. A typical CW $g^{(2)}(\tau)$ measurement showing a characteristic dip with $g^{(2)}(0)$ of 0.34 ± 0.02 is shown in Figure 5.2. This value is limited by the 532 ps jitter of the used detectors.

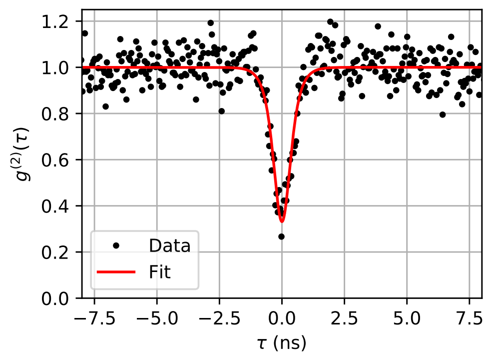

Figure 5.2: *Result of a CW HBT measurement of the QD light, for* 3.2 nW*. The fit shows a dip of* 0.34 ± 0.02.

The depth of this dip would be a direct measure of the purity of the single photon source, for jitter-free detectors. The purity of the single photon source can be studied as function of the excitation power to determine the optimum for high purity and high brightness of the single photon source. The excitation power is measured with a power meter in remote detection and converted to an estimate of the power in front of the objective. Figure 5.3a shows the fitted $g^{(2)}(0)$ as function of the excitation power in front of the objective. This measurement was done for both CW excitation configurations without and with the EOM in the setup. These two measurements were done on two different days and show different results. For both measurements, the laser was not locked. This can cause the QD to drift, reducing the contrast between between the single photon source and the background. The setup was realigned at the start of the second measurement day. The measurement where the EOM was included in the setup shows in general a higher purity, which suggests that the EOM does not limit the CW excitation.

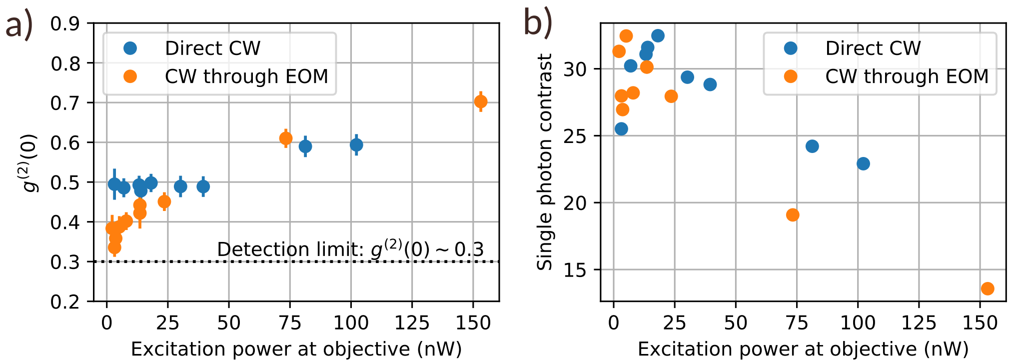

Figure 5.3: *(a) Measurement of $g^{(2)}(0)$ versus excitation power under CW excitation. (b) Single photon contrast versus excitation power. The blue dots were measured without the EOM in the setup, on 20-07-2022. The orange dots were measured through the EOM, operating at the maximum around $V_{DC} = 0$, on 21-07-2022.*

Figure 5.3a shows that the purity of the single photon source decreases for higher excitation powers. This result agrees with earlier measurements, and can be explained by imperfect laser extinction, as also suggested by the single-photon vs background contrast in Figure 5.3b decreasing for high excitation powers [5, 23]. The minimal measured $g^{(2)}(0) \sim 0.34 \pm 0.02$ is limited by the timing jitter of the detectors. The timing jitter limits the depth of the dip, as is illustrated in Figure 5.4. An old TCSPC measurement of the detectors which were used showed a jitter of approximately 532 ps. A more recent TCSPC measurement showed a jitter of 650 ps. However, it is unclear if this recent measurement can be fully trusted. It can be determined that the detection limit for a photon source with a linewidth-estimated lifetime of 0.56 ns is $g^{(2)}(0) \sim 0.26$ for a 532 ps jitter, and $g^{(2)}(0) \sim 0.30$ for a 650 ps jitter. This indicates that the photon source used in this thesis has an even higher purity than 1-0.34, because the measured $g^{(2)}(0)$ is close to the detection limit.

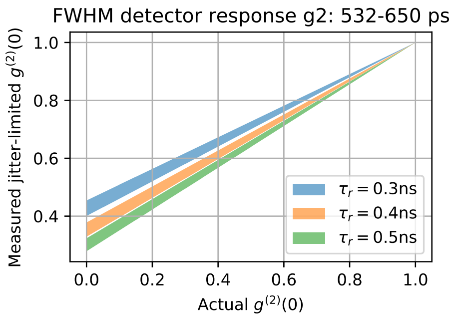

Figure 5.4: *The maximally measured dip depths in CW $g^{(2)}(\tau)$ versus the actual non-jitter-limited dip depths for detector jitters ranging from 532 ps to 650 ps, for three different lifetimes.*

5.3 Pulsed single photon correlations

With the single photon source confirmed, the EOM can be switched to pulsing mode. If the QD is addressed with sufficiently short pulses, we should detect at most one photon per pulse. This means that the second-order correlation function $g^{(2)}(\tau)$ will show peaks at intervals of the pulse period, except for $g^{(2)}(0)$, where the peak should be missing. This is because in the autocorrelation measurement in HBT setup, a single photon can only go to one of the detectors, meaning that if there is only one photon per pulse the detectors can never click at a 0 time difference. The height of the peak measured at $g^{(2)}(0)$ can thus be used to estimate the purity of the source.

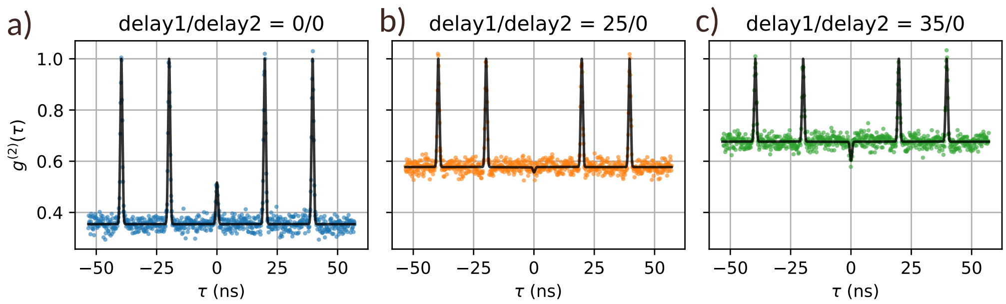

Figure 5.5: *Measurements of $g^{(2)}(\tau)$ for pulsed excitation. Data taken on 21-07-2022, for three different pulse durations. (a) has (delay1, delay2) = (0 ps, 0 ps), (b) has shorter pulses of (25 ps, 0 ps), and (c) even shorter pulses of (35 ps, 0 ps).*

Figure 5.5 shows the $g^{(2)}(\tau)$ measurements and fits for three different excitation pulse durations. It can be seen that with the decrease in pulse duration, the offset of $g^{(2)}(\tau)$ significantly increases. Since the measured light mostly contains photons emitted by the QD, this offset can not be caused by the slightly different duty cycle of the pulses. Instead, the offset is a direct measure for the amount of background light, which in this case is a significant amount. To be able to make conclusions about the purity of the single photon source, there should be little to no background light. As can be seen in Figure 5.5b,c, for the shortest pulses a dip can be measured at $g^{(2)}(0)$. This confirms a significant amount of background light, as the measured $g^{(2)}(\tau)$ is now a superposition of the CW dip and the pulsed peaks. Since this superposition is also likely present in Figure 5.5a, the actual $g^{(2)}(0)$ peak for a measurement without background light would be higher. This implies there is significant re-excitation of the QD.

The fitted $g^{(2)}(0)$ values for different delay settings of the EOM electronics are visualized in Figure 5.6 for two different analysis approaches: (i) In panel (a), the values are as shown in Figure 5.5, where we normalized the side peaks to 1. This gives the measured $g^{(2)}(0)$ values which are limited by the significant $g^{(2)}(\tau)$ offset. (ii) Panel (b), where the offset in $g^{(2)}(\tau)$ is subtracted before the normalization. This figure visualizes whether the measured $g^{(2)}(0)$ was a peak or a dip.

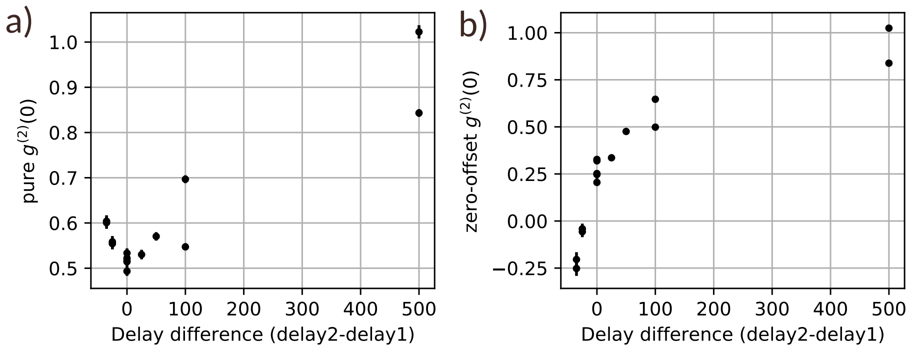

Figure 5.6: *Measurements of $g^{(2)}(0)$ for pulsed excitation, as function of the delay difference of the EOM electronics. Data taken on 21-07-2022. (a) shows the $g^{(2)}(0)$ for peaks normalized to 1, (b) shows $g^{(2)}(0)$ for offset subtracted and peaks normalized to 1.*

In Figure 5.6a it can be seen that $g^{(2)}(0)$ appears to plateau for short pulses, and even increase for the shortest pulses (small delay difference). Normally one would expect $g^{(2)}(0)$ to decrease for shorter pulses, as the re-excitation probability of the single photon source decreases. Here, due to the increasing background light, $g^{(2)}(0)$ increases for shorter pulses. This is because in the superposition of the CW dip and pulsed peaks, the CW dip is jitter-limited. If normally the peak of the pulsed excitation at $g^{(2)}(0)$ would be 0, the measured result will now show a $g^{(2)}(0) > 0$ due to the nonzero $g^{(2)}(0)$ of the jitter-limited dip.

The high background light of the measurements presented in this section can have multiple causes. One explanation could be that the extinction of the reflected laser light was not optimal, causing the measured light to contain background laser photons. However, this would add a uniform background to $g^{(2)}(\tau)$ and can not explain the measured dips. Furthermore, in the previous section, CW $g^{(2)}(\tau)$ dips with detection-limited depths were measured, indicating that the purity of the single photon light is at least ~ 0.7. Another explanation could be that the extinction ratio of the EOM was not sufficient. This would cause the QD to get excited in between the laser pulses, meaning that the background light would consist of single photons. This would explain the measured dips. Based on the EOM bias sweeps done during the measurements (Fig. 4.2b) and the minimum that was selected, the extinction ratios can be expected to be at least 100, based on the experiments of Chapter 4.

The simulations of Chapter 3 could be adapted to simulate the generation of single photon light with pulsed laser light with an extinction ratio of 100. These simulations could then assist in determining a minimum extinction ratio needed to do good pulsed excitation. The simulations could also help estimate the extinction ratio of the EOM based on the results presented in this section. Furthermore, additional experiments are required to investigate ways to improve the pulsed excitation of the QD with the EOM.

Chapter 6

Conclusions and outlook

The switching between continuous and pulsed excitation in conventional cavity-QED setups can lead to a disruption of optimal excitation settings, and often offers limited pulse tuning possibilities. A combination of a highly wavelength tunable continuous-wave laser and an electro-optic intensity modulator (EOM) allows tuning the central wavelength and pulse shape without the need for a pulsed laser. An EOM in combination with custom-built ultra-fast electronics was shown to produce tunable pulse durations in the few-hundred-ps-range, down to below 50 ps. Typical extinction ratios (ERs) of 300 (25 dB), and even up to 1000 (30 dB) were achieved. The extinction ratio collapses for pulse durations below 100 ps, but still a typical extinction ratio of 150 is achieved for the short 50 ps pulses. Further research could be done to investigate the stability of the extinction ratio over long time periods. The longer (400 ps) pulses are likely block-shaped, and further research could be done to use the fast electronics to achieve other pulse shapes. An automatic bias control was developed to lock the operating point of the EOM. A working trigger output was also developed, which at the moment of writing this thesis had a 140 ps jitter. This jitter can likely be resolved and further testing will be needed to improve the trigger output.

The EOM was incorporated in the cavity-QED setup to allow easy switching between CW and pulsed excitation. Through CW excitation of an InAs QD in a micropillar cavity, a QD with estimated lifetime of 560 ps and good purity was selected. Upon switching to pulsed excitation, second-order correlation function measurements showed both a CW dip and pulsed peaks, indicating that the single photon light contained a significant amount of background photons. A likely cause of this is that the extinction ratio of the EOM was not sufficient during the experiment.

Simulations of photon correlations were performed and proved a useful tool that can aid the understanding of the experiments. These simulations could be adapted to better understand the single photon experiments and estimate a minimal required extinction ratio. The extinction ratio of the EOM can be increased by optimizing the height of the electrical pulses. Furthermore, the possibility of placing two EOMs in series to increase the extinction ratio can also be explored, and could potentially offer great reduction of the background light.

Overall, the use of EOMs in cavity-QED setups present a promising route to more flexibility. High control over the pulses allows matching the spectral properties of the laser to the produced single photons, which opens up new possibilities for engineering of artificial photonic quantum states by quantum interference.

Version of August 23, 2022– Created August 23, 2022 - 16:39

Acknowledgements

This endeavor would not have been possible without my supervisor Wolfgang Löffler, who provided this opportunity. I would like to express my deepest gratitude to both him and Petr Steindl, who guided me in the research and provided great help and feedback on numerous accounts. I would also like to express my deepest appreciation to Alexandre Morin, for being my second supervisor and taking the time to visit my presentations and reading my thesis. I am also extremely grateful to Harry Visser and Arno van Amersfoort for taking the time to help me understand the electronics, their quick and diligent work, and for proofreading part of my thesis.

Also many thanks to Kirsten Kanneworff, Joost Vermeer, and Michiel de Dood for the useful conversations and moral support. Thanks should also go to the other members of the QO group, it was always a pleasure to be here. Finally I would like to thank everyone who brought cake to the 9th floor during my work here (counted March-August 2022): WL (4x), PS (3x), ME (2x), KK (2x), FS (2x), MD (1x) and CK (1x).

Bibliography

[1] Christopher J Chunnilall, Ivo Pietro Degiovanni, Stefan Kück, Ingmar Müller, and Alastair G Sinclair. Metrology of single-photon sources and detectors: a review. *Optical Engineering*, 53(8):081910, 2014.

[2] Jeremy L O'brien. Optical quantum computing. *Science*, 318(5856):1567–1570, 2007.

[3] Jianwei Wang, Fabio Sciarrino, Anthony Laing, and Mark G Thompson. Integrated photonic quantum technologies. *Nature Photonics*, 14(5):273–284, 2020.

[4] H Snijders, JA Frey, J Norman, MP Bakker, EC Langman, A Gossard, JE Bowers, MP Van Exter, D Bouwmeester, and W Löffler. Purification of a single-photon nonlinearity. *Nature communications*, 7(1):1–6, 2016.

[5] H Snijders, JA Frey, J Norman, VP Post, AC Gossard, JE Bowers, MP Van Exter, W Löffler, and D Bouwmeester. Fiber-coupled cavity-qed source of identical single photons. *Physical Review Applied*, 9(3):031002, 2018.

[6] P Steindl, H Snijders, G Westra, E Hissink, K Iakovlev, S Polla, JA Frey, J Norman, AC Gossard, JE Bowers, et al. Artificial coherent states of light by multiphoton interference in a single-photon stream. *Physical Review Letters*, 126(14):143601, 2021.

[7] ValeÌrian Giesz, Niccolo Somaschi, Gaston Hornecker, Thomas Grange, Bogdan Reznychenko, Lorenzo De Santis, Justin Demory, C Gomez, Isabellle Sagnes, Aristide Lemaitre, et al. Coherent manipulation of a solid-state artificial atom with few photons. *Nature communications*, 7(1):1–6, 2016.

[8] Hao Hu, Jinlong Yu, Litai Zhang, Aixu Zhang, Yan Li, Yang Jiang, and Enze Yang. Pulse source based on directly modulated laser and phase modulator. *Optics express*, 15(14):8931–8937, 2007.

[9] Adetunmise C Dada, Ted S Santana, Ralph NE Malein, Antonios Koutroumanis, Yong Ma, Joanna M Zajac, Ju Y Lim, Jin D Song, and Brian D Gerardot. Indistinguishable single photons with flexible electronic triggering. *Optica*, 3(5):493–498, 2016.

[10] R. Paschotta. Rp photonics encyclopedia. `https://www.rp-photonics.com/electro_optic_modulators.html`. RP Photonics.

[11] Electro-optical modulators operating manual. `https://www.ixblue.com/store/nir-mx950-ln-20-00-p-p-fa-fa/`, Feb 2021. iXblue.

[12] Introduction to ixblue mach-zehnder modulators bias controllers. `https://www.ixblue.com/wp-content/uploads/2021/12/introduction-to-ixblue-mbc-2019.pdf`, 2019. iXblue.

[13] Mark Fox. *Quantum optics: an introduction*, volume 15. Oxford university press, 2006.

[14] Chen-How Huang, Yung-Hsiang Wen, and Yi-Wei Liu. Measuring the second order correlation function and the coherence time using random phase modulation. *Optics express*, 24(4):4278–4288, 2016.

[15] LJ Martínez, Thomas Pelini, V Waselowski, JR Maze, Bernard Gil, Guillaume Cassabois, and Vincent Jacques. Efficient single photon emission from a high-purity hexagonal boron nitride crystal. *Physical review B*, 94(12):121405, 2016.

[16] Raimund Schneider, Christoph Biernoth, Johannes Hölzl, André Pscherer, and Joachim von Zanthier. Simulating the photon stream of a real thermal light source. *Applied Optics*, 57(24):7076–7080, 2018.

[17] Lindsey N Hillesheim and Joachim D Müller. The photon counting histogram in fluorescence fluctuation spectroscopy with non-ideal photodetectors. *Biophysical journal*, 85(3):1948–1958, 2003.

[18] Alessandro Spinelli and Andrea L Lacaita. Physics and numerical simulation of single photon avalanche diodes. *IEEE Transactions on Electron Devices*, 44(11):1931–1943, 1997.

[19] Angelo Gulinatti, Ivan Rech, Mattia Assanelli, M Ghioni, and Sergio Cova. A physically based model for evaluating the photon detection efficiency and the temporal response of spad detectors. *Journal of Modern Optics*, 58(3-4):210–224, 2011.

[20] Feiyang Sun, Yue Xu, Zhong Wu, and Jun Zhang. A simple analytic modeling method for spad timing jitter prediction. *IEEE Journal of the Electron Devices Society*, 7:261–267, 2019.

[21] Hendrik Joannes Snijders. *Quantum dot microcavity control of photon statistics*. PhD thesis, Leiden University, 2018.

[22] HJ Snijders, DNL Kok, MF Van De Stolpe, JA Frey, J Norman, AC Gossard, JE Bowers, MP Van Exter, D Bouwmeester, and W Löffler. Extended polarized semiclassical model for quantum-dot cavity qed and its application to single-photon sources. *Physical Review A*, 101(5):053811, 2020.

[23] Tessa van der Ent. polarized cavity-enhanced quantum dot-based single-photon generation. BSc Thesis, Leiden university, 2021.

[24] Jan-Philipp Jahn, Mathieu Munsch, Lucas Béguin, Andreas V Kuhlmann, Martina Renggli, Yongheng Huo, Fei Ding, Rinaldo Trotta, Marcus Reindl, Oliver G Schmidt, et al. An artificial rb atom in a semiconductor with lifetime-limited linewidth. *Physical Review B*, 92(24):245439, 2015.

Appendix I

Pulse durations for the unstable positive bias minimum

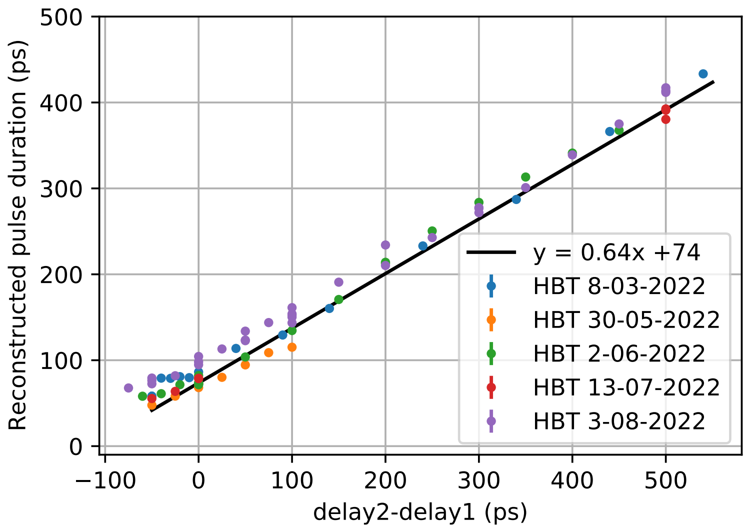

Figure I.1: *The reconstructed pulse durations for Gaussian pulse assumptions. The colors indicate data taken at different dates. The solid black line indicates a linear fit through the Gaussian-ansatz data. The purple data was measured in the positive DC bias minimum, which showed significant drifting during the measurements. Because of this, it was decided not to include this data in the main text, and limit the study to the more stable negative bias minimum.*

Appendix II

Possible causes for the trigger jitter

The TCSPC measurements of Section 4.5 appeared to show a significant 140 ps jitter in the trigger signal of the fast pulser electronics. Since these measurements, the ELD has now also measured the jitter by using an oscilloscope, and has estimated the jitter to be around 200 ps.

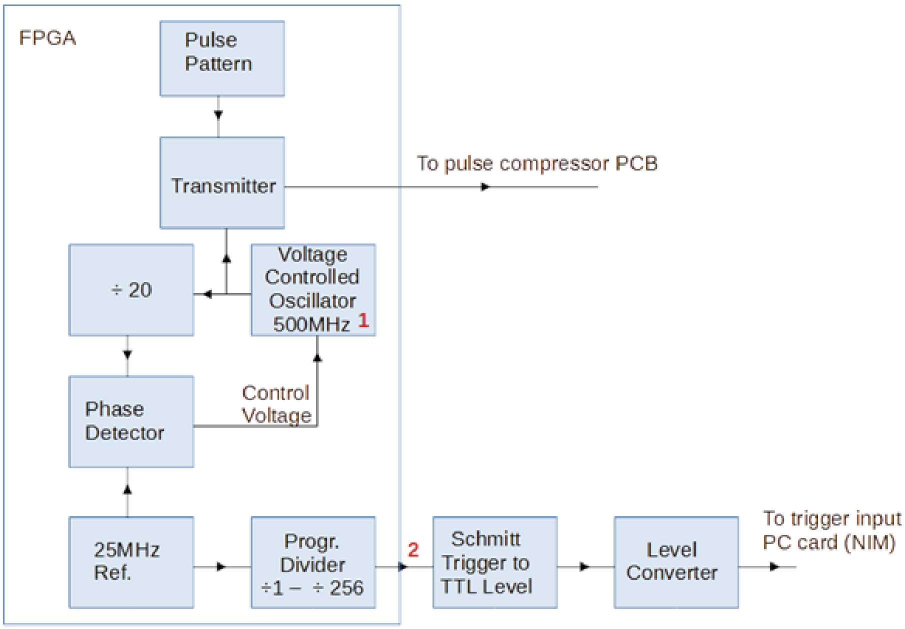

Figure II.1: *A detailed schematic of the electronics surrounding the trigger pulse. The red 1 and 2 indicate possible sources of jitter. Figure provided by Harry Visser from the ELD.*